PCCP

Cite this: *Phys. Chem. Chem. Phys.*, 2011, **13**, 18447–18467

www.rsc.org/pccp

PERSPECTIVE

Time-resolved photoelectron spectroscopy: from wavepackets to observables

Guorong Wu,†[a] Paul Hockett†[a] and Albert Stolow*[ab]

Received 21st June 2011, Accepted 17th August 2011
DOI: 10.1039/c1cp22031d

Time-resolved photoelectron spectroscopy (TRPES) is a powerful tool for the study of intramolecular dynamics, particularly excited state non-adiabatic dynamics in polyatomic molecules. Depending on the problem at hand, different levels of TRPES measurements can be performed: time-resolved photoelectron yield; time- and energy-resolved photoelectron yield; time-, energy-, and angle-resolved photoelectron yield. In this pedagogical overview, a conceptual framework for time-resolved photoionization measurements is presented, together with discussion of relevant theory for the different aspects of TRPES. Simple models are used to illustrate the theory, and key concepts are further amplified by experimental examples. These examples are chosen to show the application of TRPES to the investigation of a range of problems in the excited state dynamics of molecules: from the simplest vibrational wavepacket on a single potential energy surface; to disentangling intrinsically coupled electronic and nuclear motions; to identifying the electronic character of the intermediate states involved in non-adiabatic dynamics by angle-resolved measurements in the molecular frame, the most complete measurement.

1 Introduction

Non-adiabatic excited state dynamics of polyatomic molecules involve complex processes which redistribute both energy and charge. These processes lie at the very heart of chemistry: the making and breaking of chemical bonds. The coupling between vibrational and electronic degrees of freedom in electronically excited molecules leads to radiationless and often ultrafast processes, including internal conversion, isomerization, proton and electron transfer, and so on.[1–6] Non-adiabatic dynamics underlie the photochemistry of almost all polyatomic molecules,[7] and are important to photobiological processes, such as vision[8] and photosynthesis.[9] To study these non-adiabatic dynamics in detail, a variety

[a] *Steacie Institute for Molecular Sciences, National Research Council, 100 Sussex Drive, Ottawa, Ontario K1A 0R6, Canada. E-mail: albert.stolow@nrc.ca*
[b] *Department of Chemistry, Queen's University, Kingston, Ontario K7L 3N6, Canada*
† These authors contributed equally to this work.

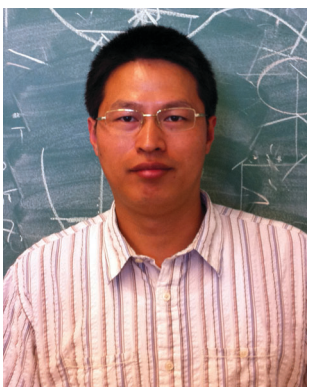

Guorong Wu

Guorong Wu obtained his BS degree from University of Science and Technology of China in 1998. He earned his PhD in 2005 at Dalian Institute of Chemical Physics and became an assistant professor at the same institute. He mainly focused on the experimental study of photodissociation dynamics and molecular reaction dynamics using high energy-resolved methods. He moved to National Research Council Canada as a Research Assistant in 2007. His current research has centered at nonadiabatic dynamics of excited polyatomic molecules using time-resolved methods, as well as quantum control of molecular dynamics with short laser pulses.

Paul Hockett

Paul Hockett earned his PhD in 2008 from Nottingham University, UK, under the supervision of Katharine Reid. His thesis work was on the photoionization dynamics of polyatomic molecules. Paul moved to the Steacie Institute for Molecular Science, National Research Council of Canada, as a Research Associate in 2009. His research interests include time-resolved photoelectron spectroscopy, ultra-fast dynamics, molecular alignment and strong field processes.

of experimental methods have been developed. They can generally be classified into two categories: energy-resolved measurements and time-resolved measurements. In the former case, the internal state distribution, translational energy distribution, and angular distribution of the final chemical reaction products are measured. The excited state dynamics of the molecule are often indirectly inferred from these measurements, usually in concert with high-level theoretical calculations. Time-resolved measurements, founded upon seminal studies of A. H. Zewail and co-workers,[10–12] directly follow the flow of vibrational energy and/or charge within molecular systems during these processes, ideally allowing observation of both structural and electronic rearrangements during chemical reactions, following excitation. Unified pictures involving both energy-resolved and time-resolved measurements are often required in order to provide the most detailed information on molecular dynamics. In the following, we consider only time-resolved measurements.

In time-resolved studies of molecular dynamics, an ultrafast pump pulse is used to prepare an excited state wavepacket, the evolution of which is observed by interaction with a time-delayed probe pulse. The probe pulse projects the evolving wavepacket onto a set of final states which act as a template. The amount of information obtained from these experiments is very much dependent on the final state(s) selected. A variety of probing methods have been developed, such as nonlinear optical spectroscopy and transient absorption spectroscopy in the condensed phase, laser-induced fluorescence and resonant multiphoton ionization in the gas phase, and time-resolved X-ray or electron diffraction with ultrafast X-ray or electron pulses in both condensed and gas phases.[13–18] Here, we focus upon gas phase time-resolved photoelectron spectroscopy (TRPES) of neutral polyatomic molecules. TRPES is particularly well suited to the study of ultrafast non-adiabatic processes because photoelectron spectroscopy is sensitive to both electronic configurations and vibrational dynamics.[19] Due to the universal nature of ionization detection, TRPES can follow dynamics along the entire reaction coordinate. In TRPES experiments, a time-delayed probe laser generates a free electron *via* photoionization of the evolving excited state, and the electron kinetic energy and angular distribution are measured as a function of time. As a probe, TRPES has several practical and conceptual advantages:[20]

1. Ionization is always an allowed process, with relaxed selection rules due to the allowed range of symmetries of the outgoing electron. Any molecular state can be ionized, hence there are no dark states in photoionization.

2. Highly detailed, multiplexed information can be obtained by differentially analyzing the outgoing photoelectron with respect to kinetic energy and emission angle.

3. Charged-particle detection is extremely sensitive.

4. Detection of the ion provides mass information on the carrier of the spectrum.

5. Higher order (multiphoton) processes, which can be difficult to discern in other fs experiments, are readily revealed.

6. Photoelectron–photoion coincidence measurements can allow for studies of cluster solvation effects as a function of cluster size and for time-resolved studies of scalar and vector correlations in photodissociation dynamics.

7. The final state(s) in TRPES, the ground or low-lying excited electronic states of the cation, are usually well characterized from other photoionization studies (*e.g.* HeI photoelectron spectra) or theoretical calculations.

TRPES has been the subject of a number of reviews[21–33] and these cover various aspects of the field. Here, we intend to give a pedagogical overview of TRPES and its application to non-adiabatic excited dynamics in polyatomic molecules. We aim not only at readers who are already somewhat familiar with the field, but also at a more general audience, particularly new researchers and graduate students. Therefore, a significant amount of background is included and is, necessarily, somewhat lengthy. Readers with a grounding in molecular dynamics and TRPES should feel free to skim or skip some parts. The subsequent sections of this paper are arranged as follows. In Section 2, a conceptual framework for time-resolved photoionization measurements is presented, followed by more detailed discussion of the underlying theory. Emphasis is placed on understanding excited state dynamics and following these dynamics with TRPES. The salient points are illustrated with simple model examples, which provide intuitive and faithful pictures illustrating the important concepts. In Section 3, a brief introduction to TRPES experimental techniques is given, followed by three prototypical experimental examples chosen to highlight the application of TRPES to different problems: from the simplest vibrational wavepacket on a single potential energy surface, to disentangling intrinsically coupled electronic and nuclear motions, to identifying character of the intermediate states involved in dynamics by making measurements in the molecular frame—the most complete measurement. We end with a short conclusion and outlook.

Albert Stolow

Albert Stolow is a Principal Research Officer within the Steacie Institute for Molecular Sciences, National Research Council and Program Leader of the Molecular Photonics Group. He is Adjunct Professor of Chemistry and Adjunct Professor of Physics at Queen's University in Kingston and Adjunct Professor of Physics at the University of Ottawa. His group's research interests include ultrafast molecular dynamics and quantum control, non-linear optical spectroscopy, molecular strong field physics and applications, and non-linear microscopy of live cells.

2 Background and theory

We present here a pedagogical overview of the important aspects of excited state dynamics—the behaviour of wavepackets—and discuss how such wavepackets can be probed *via* photoionization. A conceptual framework for time-resolved photoionization measurements is presented (Section 2.1),

followed by more detailed discussion of the underlying theory (Sections 2.2–2.5). We pay special attention to the photoelectron angular distribution (PAD), which is a very powerful but complex and, consequently, often ignored observable. In these latter sections, key formulae are presented, but the emphasis remains on physical intuition. The mathematics is chosen to illustrate fundamental concepts but is not derived or explored in depth. Detailed technical discussion is beyond the scope of this article, nor do we aim to duplicate the contents of many recent review articles on non-adiabatic dynamics and time-resolved photoelectron spectroscopy. See, for example, ref. 4, 6 and 34 for detailed discussion of dynamics and conical intersections, and ref. 26, 33, 35 and 36 for further details and derivations of TRPES theory.

2.1 Pump–probe methodology and zeroth-order framework

In any time-resolved experiment, we require three key components:[12,35,37]

1. A well-defined start time, t_0.
2. A well-defined time delay, Δt, during which the system evolves in a field-free environment.
3. A well-defined probe time, $t_{probe} = t_0 + \Delta t$, at which the system is interrogated, producing an observable.

Here we are interested in excited state molecular dynamics. In this case, a pump–probe photoionization measurement represents an excellent scheme, fulfilling the above requirements.[23,29,35,38] Fig. 1 illustrates such a scheme. First, a pump laser pulse excites the molecule from its ground state to an electronically excited state. The pump pulse defines t_0 to within the duration of the pulse. The pump pulse prepares a wavepacket, a coherent superposition of the exact molecular eigenstates (see Section 2.2), which evolves in the excited state during the field-free interval Δt. Next, a probe pulse at $t_{probe} = t_0 + \Delta t$ interrogates the molecule *via* photoionization; this process can be envisaged as the excited state coupling with, or projecting onto, the molecular ionization continuum, itself composed of the molecular ion and the ejected photoelectron. Ionization occurs within the duration of the probe pulse, defining t_{probe} to within this window. Finally, the photoelectron is detected, yielding a pump–probe signal dependent on Δt. The measurement of the emitted electron may additionally be energy and angle-resolved for maximum information.

In this context, *dynamics* signifies the response of the molecule to the pump pulse; this response can be further classified as a photo*physical* or photo*chemical* process,[7] broadly differentiating between intramolecular processes which eventually return the molecule to the ground state, and those which produce chemical changes. Examples of photophysical processes include internal conversion, intersystem crossing, fluorescence and phosphorescence. Examples of photochemical processes include dissociation, isomerization, proton transfer and charge transfer.

The time evolution of excited states of molecules is, in general, very complex due to the strong and rapid coupling of nuclear and electronic degrees of freedom.[6,7,34,35,39] However, we can make approximations which enable us to consider the dynamics in a more physically transparent picture. In particular, we turn to the Born–Oppenheimer (B–O) approximation.

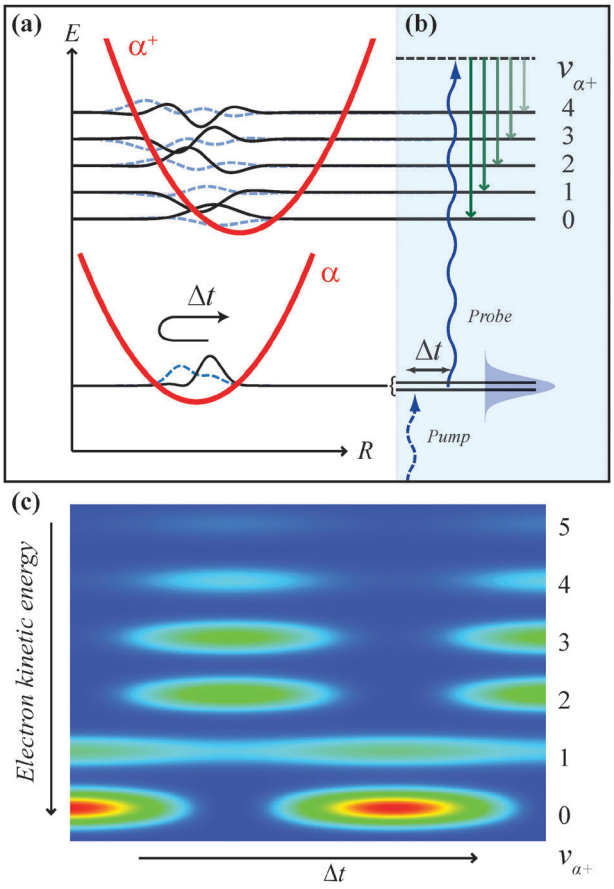

Fig. 1 Time-resolved pump–probe photoelectron spectroscopy. (a) Schematic picture of wavepacket motion, and wavefunction overlap with a set of final ion states. A two-level wavepacket on a harmonic potential surface α is shown for t_0 (solid line) and Δt (dashed line), for details see Section 2.2. Vibrational wavefunction overlap with ionic vibrational levels $v_{\alpha+}$, at t_0 (solid line) and Δt (dashed line), is shown on the upper surface; integration of these functions over R gives Franck–Condon factors (see Section 3.2.1). (b) Energy-level diagram for the pump–probe scheme. The pump pulse populates two vibrational eigenstates, v_α, which fall within the bandwidth of the pulse; these eigenstates constitute the wavepacket illustrated in panel (a). The probe pulse, at Δt, projects the wavepacket onto the ionization continuum. The photon energy is partitioned between the outgoing photoelectron and the ion, in this example populating vibrational levels $v_{\alpha+}$. Time and energy resolved detection of the photoelectron provides the TRPES shown in (c), which has energy bands corresponding to the ion vibrational states, and time-dependence determined by the wavepacket motion. Different bands in the TRPES show different time-dependence, as determined by the final state wavefunctions.

This is an adiabatic separation of the light, fast moving electrons from the heavy, slow moving nuclei; in effect, we assume that the electrons can instantaneously adjust to the motion of the nuclei. This allows us to write the full wavefunction of the molecule as a product of the electronic and nuclear wavefunctions. Within this framework, we can make further assumptions: for instance, that the vibrational and rotational wavefunctions are separable[33,40] (*i.e.* there is no interaction between these motions), that spin can be neglected and so on. Following the separation of rotations, we can choose to work in

the molecular frame (MF) for simplicity‡, and hence write the full molecular wavefunction as:

$$\Psi = \Phi_\alpha(r;R)\psi_{v_\alpha}(R) \quad (1)$$

where r represent electronic coordinates and R nuclear coordinates. We follow the notation of ref. 33 and denote the electronic wavefunction Φ_α and vibrational wavefunction ψ_{v_α}; the subscripts allow indexing of different electronic states α and vibrational levels within each state v_α.

This separation allows the conceptualization of electronic states in terms of potential energy surfaces,[7,39] the mapping of the electronic energy of the system as a function of nuclear coordinates as defined by the (electronic) Schrödinger equation:

$$H_{\text{elec}}(r;R)\Phi_\alpha(r;R) = E_\alpha(R)\Phi_\alpha(r;R) \quad (2)$$

where $H_{\text{elec}}(r;R)$ is the electronic part of the Hamiltonian and $E_\alpha(R)$ the electronic energy. By solving this equation for various nuclear configurations, that is various R, the potential energy surface is mapped; the harmonic potentials shown in Fig. 1 are an example of such surfaces. The nuclei move within the potential defined by $E_\alpha(R)$, so will respond to the topography of the potential energy surface; energy is exchanged between potential and kinetic energies as the surface is explored by the nuclei.

In a classical picture, we can consider trajectories on the potential energy surface akin to a ball bearing, released at some initial point, rolling around the surface;[43] in a quantum mechanical picture, we can consider a wavepacket (see Section 2.2), created on some region of the surface, exploring the topography.[6,7,43] In either picture, the initial population of some region of the excited state is determined by excitation from the ground state, as induced by the pump laser at t_0. Adiabatic molecular dynamics, by definition on a single excited state surface, is described entirely within the B–O picture.

Non-adiabatic processes occur when different B–O surfaces are coupled by vibrational motions.[44] In this case we can visualize the trajectory (or some "fraction" of the wavepacket) crossing from one surface to another,[7,37,45,46] hence changing the electronic state of the system from, *e.g.*, α to β. This concept is illustrated in Fig. 2. By definition, the coupling represents a breakdown in the B–O approximation, but the B–O picture is still useful provided that the surface is well-described by it in all other regions of configuration space. In polyatomic molecules, points of intersection (degeneracy) of B–O surfaces are termed conical intersections, and these form seams of intersection in multidimensional coordinate space.[6,34] In the region of intersection, nuclear and electronic motions are strongly coupled.

In a somewhat more precise description, we can regard the B–O approximation as a particular case of a *zeroth-order* treatment, in which a simplified Hamiltonian, H_0, is used to provide zeroth-order eigenstates[33,39,40] (more correctly, basis functions) which can be used to approximate (for a little while)

‡ Although experimental results are, by definition, in the lab frame, there is no loss of generality here as a laboratory frame measurement can be related to the convolution of the molecular frame result with the molecular axis distribution.[31,41,42]

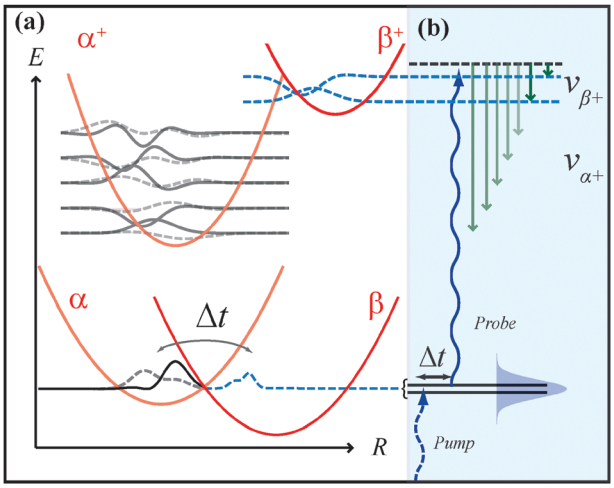

Fig. 2 Conceptual overview of TRPES with two coupled electronic states having complementary Koopmans' correlations, *i.e.* $\alpha \rightarrow \alpha^+$ and $\beta \rightarrow \beta^+$ upon ionization. (a) As in Fig. 1(a), a two-level wavepacket on a harmonic potential surface α is shown for t_0 (solid line) and Δt (dashed line); vibrational wavefunction overlap with ionic vibrational levels, at t_0 (solid line) and Δt (dashed line), is shown on the upper surface. In the case of coupled surfaces, the wavepacket bifurcates as it evolves in the region of strong coupling, leading to population on β. (b) Energy level diagram for the pump–probe scheme. As in Fig. 1(b), photon energy is partitioned between the outgoing photoelectron and ionic vibrational levels. In this case, vibrational levels in both α^+ and β^+ are populated upon ionization. Time and energy resolved detection of the photoelectron in this case would be similar to Fig. 1(c), but with additional low electron energy bands appearing at later Δt as population appears on β, hence ionization populates levels $v_{\beta+}$.

the exact eigenstates. The zeroth-order B–O states (eqn (1)) are solutions to a H_0 which is derived from an adiabatic approximation to the full molecular Hamiltonian, H,[39,40] providing approximate eigenstates composed of separable electronic and nuclear wavefunctions.§ In the limit of frozen nuclei, the B–O states are exact. Adiabatic dynamics arise due to the parametric dependence of the electronic wavefunction on the nuclear coordinates, whereas non-adiabatic dynamics are ascribed to the couplings between zeroth-order states due to the neglected terms in H.[34,40]¶ In studying non-adiabatic molecular dynamics, we are therefore most interested in probing both the *nuclear and electronic structure* of the excited state molecule as a function of time. With these aims in mind, photoionization represents an ideal probe because it is sensitive to both the nuclear and electronic degrees of freedom.

The probing of an excited state wavepacket *via* photoionization can also be conceptualized by making use of the B–O wavefunctions.[33] Furthermore, the Franck–Condon (FC)

§ This is achieved by neglecting the nuclear kinetic energy operator which couples nuclear and electronic motions in the full Hamiltonian, although other terms are also often neglected. For further discussion see for example ref. 34, 39, 40 and 47.

¶ Another set of physically meaningful zeroth-order basis states are the diabatic states, obtained by unitary transformation of the adiabatic states into a representation in which the nuclear kinetic energy operator is diagonal. Such states are then coupled by off-diagonal potential energy terms. The diabatic states can also be used in the region of conical intersections where the B–O approximation fails.[4,6]

principle may be invoked to allow complete separability of the vibrational and electronic contributions to the ionization matrix elements. This leads to the concepts of Koopmans' correlations, pertaining to the electronic wavefunctions, and Franck–Condon factors, pertaining to the vibrational wavefunctions. Section 2.3 treats these concepts in more detail; in the remainder of this section we continue to sketch a conceptual overview.

The Koopmans picture is essentially an independent-electron molecular orbital approximation (*cf.* Hartree–Fock approach) applied to ionization. For a system containing N electrons, the electronic wavefunction of the excited state, $\Phi_\alpha(r;R)$, is considered as an expansion in N one-electron orbitals. The process of ionization removes a single electron from one of these orbitals, creating an ion in a specific $(N-1)$-electron configuration. Upon photoionization, a particular excited electronic state of the neutral is therefore correlated directly with a specific final electronic state of the ion.‖ Fig. 2 shows this concept, with ionization from Φ_α resulting in formation of $\Phi_{\alpha+}$ and, similarly, $\Phi_\beta \rightarrow \Phi_{\beta+}$. This limiting case, in which different excited electronic states correlate with different electronic states of the ion, can be termed a *complementary* ionization correlation;[48] the other limiting case, where Φ_α and Φ_β correlate with the same final electronic state, can be termed a *corresponding* ionization correlation.[49] Hence, if the electronic character of the neutral evolves due to nuclear motions during the experimental window Δt, we expect, in the case of complementary ionization correlations, to see different final *electronic* states populated upon ionization as a function of time. This may be observable in the TRPES as the appearance of a band in the photoelectron spectrum at a different energy. In the case of corresponding ionization correlations, the evolution of the electronic character of the excited state may, or may not, be so easily determined from the TRPES, depending on details such as geometry changes upon photoionization.

Franck–Condon (FC) factors are the square of the purely vibrational overlap integrals between the initial and final vibrational wavefunctions. Within the FC approximation, we have an intuitive picture of vibrational level population of the ion upon photoionization. If the ionic geometry is similar to that of the excited state, we expect good overlap when $\psi_{v_{\alpha+}}$ is similar to ψ_{v_α}, hence the FC factors favour small changes in the vibrational quantum number, that is transitions with small Δv dominate, where $\Delta v = v - v_+$. Therefore, short vibrational progressions will be observed in the photoelectron spectrum. Conversely, a different ionic equilibrium geometry leads to non-zero overlap with many $\psi_{v_{\alpha+}}$. A range of Δv transitions are expected, producing long vibrational progressions in the spectrum. Furthermore, evolution of the wavepacket on the excited state, and/or changes in its vibrational composition due to non-adiabatic couplings, will be reflected in the vibrational (Franck–Condon) structure of the photoelectron spectrum. In the case of corresponding ionization correlations, the vibrational structure may still carry information on non-adiabatic electronic state couplings: if the prepared state couples to a lower lying electronic state, energy conservation dictates that highly vibrationally excited levels in this lower state will be populated, and therefore the vibrational band structure of the TRPES will evolve. Such changes are not as dramatic as electronic band structure changes, but may still be enough to determine non-adiabatic electronic population dynamics.[49] However, changes in the TRPES vibrational structure may also signify other (adiabatic) dynamical processes, such as intramolecular vibrational energy redistribution (IVR).[50]

The approximations discussed above offer a relatively intuitive conceptual framework within which excited state dynamics, probed *via* photoionization, can be visualized. In the following sections, we explore the concepts introduced here in more detail, offering model systems which give insight into the prototypical experimental results discussed in Section 3.

2.2 Wavepacket dynamics

The eigenstates of a system are, by definition, stationary: they do not evolve in time. However, a time-dependent state can be formed from a linear combination of time-independent eigenstates. The coherent superposition of basis states is called a wavepacket,[6,51–53]

$$|\Psi(t)\rangle = \sum_n A_n e^{-i[E_n t/\hbar + \phi_n]} |\psi_n\rangle \qquad (3)$$

Here the wavepacket, $|\Psi(t)\rangle$, is described as a linear combination of exact eigenstates $|\psi_n\rangle$, with a time-dependent phase given by $e^{-i[E_n t/\hbar + \phi_n]}$, where E_n is the energy of the eigenstate and ϕ_n the phase at $t = 0$, and expansion coefficients A_n. The A_n are the amplitudes of each $|\psi_n\rangle$ in the superposition, and are related to the pump pulse which prepares the wavepacket.[35,54] An important point here is that the A_n are time-independent for an isolated system because there are no couplings between the eigenstates $|\psi_n\rangle$: the amplitude of each eigenstate in the superposition remains constant in time, and it is only their phases which evolve.

In general, we do not know the exact eigenstates and must resort to the approximate eigenstates of a simplified Hamiltonian, such as the B–O states discussed above. The terms in the Hamiltonian neglected by the approximation will lead to evolution (coupling) of the approximate eigenstates. If we were to express the wavepacket in terms of the approximate eigenstates, the couplings between the approximate $|\psi_n\rangle$ will cause A_n to become time dependent, *i.e.* $A_n \rightarrow A_n(t)$. In the B–O basis, non-adiabatic couplings will lead to evolution in the $A_n(t)$ as population is transferred between the states.[4,6,51,55] This will be most probable in regions where states are strongly interacting, such as at conical intersections.

To put this idea on a more solid physical foundation, consider a diatomic molecule in which a two-state wavepacket is created, composed of the first two vibrational levels. We assume that the system is well-described as a harmonic oscillator, with potential of the form**

$$V(R) = \tfrac{1}{2}R^2 \qquad (4)$$

‖ For simplicity we assume here a single-configuration description, but the same picture may be applicable to multi-configuration cases, see for example Section 3.2.2 and Fig. 10.

** Note that the equations presented here have been simplified by using atomic units, that is setting $k = m = \omega = h = 1$, because we are only interested in the form of the solutions, not quantitative values.

where R is defined as the displacement from the equilibrium bond length R_e. The eigenstates of the harmonic oscillator Hamiltonian are in the form of the Hermite polynomials $H_v(R)$, where v is the number of vibrational quanta:

$$\psi_v(R) = \sqrt{\frac{1}{2^n v! \pi^{\frac{1}{2}}}} e^{-\frac{R^2}{2}} H_v(R) \quad (5)$$

The wavefunctions $\psi_0(R)$ and $\psi_1(R)$ are illustrated in Fig. 3(a). The energies are given by:

$$E_v = v + \tfrac{1}{2} \quad (6)$$

From these wavefunctions, we can now set up a two-state wavepacket as defined by eqn (3) using the eigenstates $v = 0$ and $v = 1$, and setting $A_0 = A_1 = 1$ and $\phi_0 = \phi_1 = 0$:

$$\Psi(R,t) = e^{-i\pi t}\psi_0(R) + e^{-3i\pi t}\psi_1(R) \quad (7)$$

This wavepacket evolves according to the time-dependent phase factors, hence according to the energy separation of the two eigenstates. The form of the wavepacket changes as the two component eigenstates come into constructive or destructive interference. This concept is illustrated in Fig. 3(b). As the relative phase of the two components of $\Psi(R,t)$ varies, so $\Psi(R,t)$ oscillates between the sum ($t = 0$) and the difference ($t = 0.5$) of the two components. Here t is given in terms of the oscillation period, hence $t = 1$ represents a full period where the wavepacket will be identical to the case shown for $t = 0$. The probability density, $\Psi(R,t)\Psi^*(R,t)$, shows how the wavepacket is localized at different R as a function of time. The expectation value of R, given by $\langle R(t)\rangle = \langle \Psi(R,t)|R|\Psi(R,t)\rangle$, is plotted in Fig. 3(c). The expectation value oscillates, as expected from the form of $\Psi(R,t)$ shown in Fig. 3(b). Therefore, any observable sensitive to $\langle R(t)\rangle$—such as the projection of the wavepacket onto a final state *via* a probe laser pulse, detailed in Section 2.4—will show sinusoidal oscillations.

Conceptually, this two-state example illustrates the key points of wavepacket dynamics:

1. Wavepackets are composed of a superposition of a suitable set of basis states of the system which could be the exact eigenstates (if known) or, for example, zeroth-order states whose superposition can be used to approximate the exact eigenstates for a certain period of time.

2. The time-evolution of the wavepacket is dependent on its composition, as prepared by the pump laser pulse,[35,54] and the form of the potential energy surface upon which it moves.[6,7,43]

3. The time-evolution of the wavepacket is sensitive to the energy differences between the basis states due to the presence of E_n in the exponential phase factors. A time-dependent signal therefore contains information on the energy level spacings of the system which can be obtained by a Fourier transform of the pump–probe signal—an example of this is shown by the iodine photoelectron data discussed in Section 3.2.1.

4. The "shape" of the wavepacket evolves in time, so any measurement sensitive to this evolution can, in some sense, map the wavepacket and its dynamics. See, for example ref. 6, 35, 36, 43, 46 and 56 and Sections 2.3–2.5 for theory, and ref. 11, 57–60 and Section 3.2 for experimental examples.

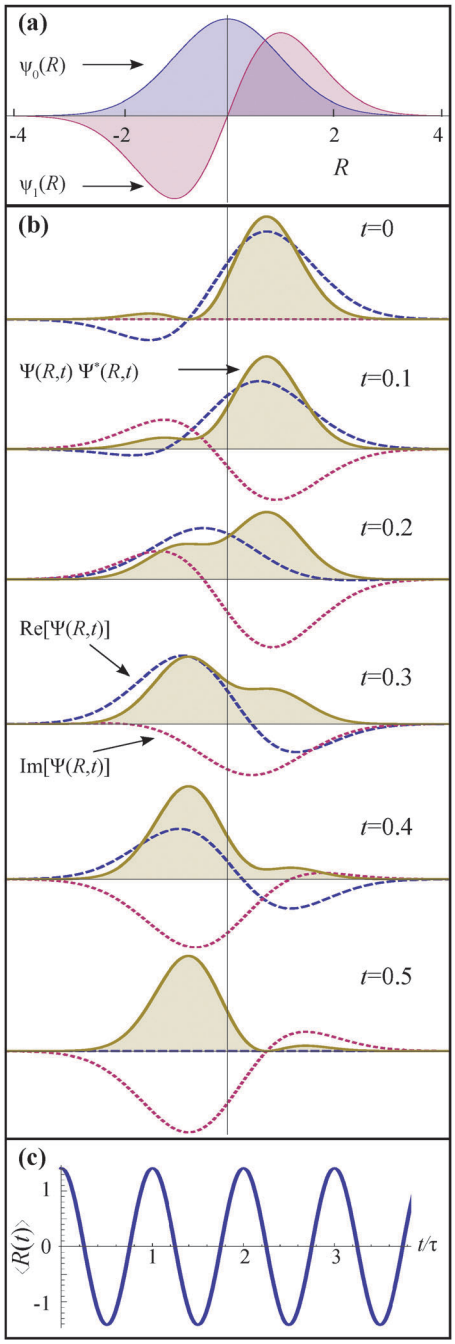

Fig. 3 (a) The harmonic oscillator wavefunctions $\psi_0(R)$ and $\psi_1(R)$, as given by eqn (5). (b) The probability density $\Psi(R,t)\Psi^*(R,t)$ (filled curve), shown at different times t, for the two-level vibrational wavepacket defined by eqn (7). Dashed and dotted lines show Re[$\Psi(R,t)$] and Im[$\Psi(R,t)$] respectively. (c) The expectation value $\langle R(t)\rangle$. The oscillations reflect the localization of probability density, moving from $x > 0$ to $x < 0$ and back, as the wavepacket evolves.

In this two-state example, the time-evolution is simple, leading to a periodic oscillation of $\Psi(R,t)$. More generally, an n-state system can display much more complex time-evolution. For a polyatomic molecule, additional complications arise because the exact molecular eigenstates are not necessarily well-described by convenient, separable functions—such as the harmonic oscillator functions used above—and

further approximations must be made in order to gain physical insight. In this very general case, the wavepacket may display apparently irreversible evolution as the system undergoes energy conversion processes, such as internal conversion or intersystem crossing. See for example ref. 4, 6, 36, 46 and 55 for further details on complex wavepacket evolution.

2.3 Photoionization and observables

As already mentioned, in considering time-resolved photoelectron measurements, we can conceive of different "levels" of observation: time-resolved photoelectron yield (equivalent to time-resolved ion yield); time and energy-resolved photoelectron yield; time, energy and angle-resolved photoelectron yield. Each type of measurement is progressively more differential, thus containing more information about the excited state wavepacket; each type of measurement is also progressively more difficult. In general, a time and energy-resolved measurement—*i.e.* TRPES—is now standard, given the commercial availability of femtosecond (fs) laser sources and a variety of possible experimental techniques (see Section 3). Time, energy and angle-resolved measurements, which provide time-resolved photoelectron angular distributions (TRPADs), are more challenging, particularly when the aim is to obtain full 3D information in the molecular frame. Such techniques are now becoming more common, with the development of various 2D, 3D and 6D (two-particle coincidence) imaging techniques (see Section 3.1).

In order to make a photoelectron measurement, the state under investigation is coupled to the ionization continuum *via* a probe laser pulse, resulting in ejection of an electron (photoionization) and population of a specific final ionic state. For this very general case, within the dipole approximation and a perturbative light–matter interaction regime (often termed the *weak field* regime), the transition moment can be written as:[61]

$$d_{\mathrm{i}\rightarrow\mathrm{f}} = \langle \Psi_{\mathrm{f}}(R,r);\Psi_{\mathrm{e}}(\boldsymbol{k};R,r)|\hat{\boldsymbol{\mu}}\cdot\boldsymbol{E}_{\mathrm{probe}}|\Psi_{\mathrm{i}}(R,r)\rangle \qquad (8)$$

Here the subscripts i, f, e denote the initial, final and photoelectron wavefunctions, respectively, $\hat{\boldsymbol{\mu}}$ is the dipole operator and $\boldsymbol{E}_{\mathrm{probe}}$ is the incident radiation field.†† Eqn (8) is referred to as the photoionization (or dipole) matrix element. We can envisage this matrix element as describing the projection, or mapping, of the N-electron Ψ_{i} onto the ionization continuum, comprised of the final (ionic) state of the $(N-1)$-electron system Ψ_{f}, and the outgoing photoelectron $\Psi_{\mathrm{e}}(\boldsymbol{k})$ with wavevector $\boldsymbol{k}$. Observables are determined by the square of this matrix element. In order to simplify the notation, the dependence of these wavefunctions on $(R,r,\boldsymbol{k})$ is generally omitted from the following treatment, unless critical to the discussion.

†† We have neglected the time-dependence of the laser pulse from the ionization matrix element as defined in (8). This matrix element therefore applies exactly for a delta-function (instantaneous) pulse, it can also be considered a good approximation for the case where the dynamics are longer than the timescale of the probe pulse.[33] More generally the time-dependence of the laser field can be included explicitly in the matrix element[35,62] and, in the perturbative regime, this can be factored into the matrix element of eqn (8) and a laser dependent function.[33,35,61,62]

In the context of a time-resolved pump–probe measurement, the "initial" state for probing *via* photoionization corresponds to the neutral excited state prepared by the pump laser pulse. The "initial" state of the system is therefore a time-dependent wavepacket, as discussed in Section 2.2, and the photoionization matrix element can be expanded in terms of the basis states of the system using eqn (3):

$$\begin{aligned} d_{\mathrm{i}\rightarrow\mathrm{f}}(t) &= \langle \Psi_{\mathrm{f}};\Psi_{\mathrm{e}}|\hat{\boldsymbol{\mu}}\cdot\boldsymbol{E}_{\mathrm{probe}}|\Psi_{\mathrm{i}}(t)\rangle \\ &= \sum_n A_n(t)\mathrm{e}^{-i[E_n t/\hbar+\phi_n]}\langle \Psi_{\mathrm{f}};\Psi_{\mathrm{e}}|\hat{\boldsymbol{\mu}}\cdot\boldsymbol{E}_{\mathrm{probe}}|\psi_n\rangle \\ &= \sum_n A_n(t)\mathrm{e}^{-i[E_n t/\hbar+\phi_n]}d_{n\rightarrow\mathrm{f}} \end{aligned} \qquad (9)$$

Here the $d_{n\rightarrow\mathrm{f}}$ are the time-independent basis state ionization matrix elements. As discussed in Section 2.2, we write the A_n as time-dependent in order to allow for modelling of wavepacket dynamics without knowledge of the exact eigenstates. From this form of the photoionization matrix element, it is clear that the time-dependence of the $d_{\mathrm{i}\rightarrow\mathrm{f}}(t)$ is a mapping of the time-dependence of the excited state through the "filter" of photoionization.

Generally, as shown in eqn (8), the matrix elements $d_{n\rightarrow\mathrm{f}}$ are both coordinate and energy dependent, so the response of $d_{\mathrm{i}\rightarrow\mathrm{f}}(t)$ to the wavepacket may be very complicated. A typical approach towards interpreting experimental data is therefore to make further simplifications, for instance application of the B–O approximation (see below), the Franck–Condon approximation, and the assumption of the independence of the matrix elements on photoelectron energy. Useful qualitative pictures can usually be gained from experimental data in this manner, even if the approximations are not strictly valid. Therefore, although the photoionization matrix elements are, in general, unknown (and are indeed very difficult to calculate *ab initio*), in many cases the mapping of the time-dependence onto the observable means that the precise details are not required in order for a time-resolved experiment to provide useful information on excited state dynamics. Experimental examples and interpretations will be discussed in Section 3.

As discussed in Section 2.1, it is often desirable to work within the B–O framework in order to provide a physically insightful picture of both excited state dynamics and the mapping of these dynamics onto observables. Within the B–O picture, we can write the ionization matrix elements as separate electronic and vibrational wavefunctions:

$$d_{\mathrm{i}\rightarrow\mathrm{f}} = \langle \Phi_{\alpha+}\psi_{v_{\alpha+}};\Psi_{\mathrm{e}}|\hat{\boldsymbol{\mu}}\cdot\boldsymbol{E}_{\mathrm{probe}}|\Phi_{\alpha}\psi_{v_{\alpha}}\rangle \qquad (10)$$

where, as previously, α indexes the electronic state, v_α the vibrational level and + denotes states of the ion. This equation can be further separated by application of the Franck–Condon (FC) principle:

$$d_{\mathrm{i}\rightarrow\mathrm{f}} = \langle \psi_{v_{\alpha+}}|\psi_{v_{\alpha}}\rangle\langle \Phi_{\alpha+};\Psi_{\mathrm{e}}|\hat{\boldsymbol{\mu}}\cdot\boldsymbol{E}_{\mathrm{probe}}|\Phi_{\alpha}\rangle \qquad (11)$$

The FC approximation is the assumption of nuclear coordinate independence of the ionization matrix element. This approximation requires that, over some range of R, both the initial and final electronic states are coordinate independent, *i.e.* $\Phi(R,r) \rightarrow \Phi(r)$.[63]

Eqn (11) can also be written in terms of a time-dependent initial state, now expressed in the B–O basis functions:

$$d_{i\to f}(t) = \sum_{\alpha,v_\alpha} A_{\alpha,v_\alpha}(t)e^{-i\left[E_{\alpha,v_\alpha}t/\hbar+\phi_{\alpha,v_\alpha}\right]}\langle\psi_{v_{\alpha+}}|\psi_{v_\alpha}\rangle \times \langle\Phi_{\alpha+};\,\Psi_e|\hat{\boldsymbol{\mu}}\cdot\boldsymbol{E}_{probe}|\Phi_\alpha\rangle \quad (12)$$
$$= \sum_{\alpha,v_\alpha} A_{\alpha,v_\alpha}(t)e^{-i\left[E_{\alpha,v_\alpha}t/\hbar+\phi_{\alpha,v_\alpha}\right]}d_{\alpha,v_\alpha\to f}$$

Here the $d_{\alpha,v_\alpha\to f}$ take the same role as the $d_{n\to f}$ given above. This form of the ionization matrix elements shows mathematically the concepts discussed in Section 2.1. The square of the vibrational overlap integrals $\langle\psi_{v_{\alpha+}}|\psi_{v_\alpha}\rangle$ are the Franck–Condon factors which describe the vibrational structure of the photoelectron spectrum. The electronic part of the matrix element describes the dipole coupling between the initial state, Φ_α, and final product state, $\Phi_{\alpha+},\Psi_e$, which, in a molecular orbital treatment, leads to the Koopmans' correlations between α and $\alpha+$. The electronic part of the ionization matrix element therefore describes the electronic band structure of the photoelectron spectrum. The photoelectron (continuum) wavefunction has not explicitly been discussed so far, but is important when measuring photoelectron angular distributions (PADs), and will be discussed further in Section 2.5. The approximations required to develop this picture are far from exact, but nonetheless provide a useful and intuitive starting point for interpretation of photoelectron spectra.

This discussion has been very general in order to outline the underlying quantum mechanics. We now proceed to discuss TRPES and TRPADs in more detail and, continuing from Section 2.2, provide simple model systems as physically insightful examples. Experimental examples following from these model systems are discussed in Section 3.

2.4 TRPES

The photoelectron spectrum is an energy resolved measurement determined by the ionization matrix elements. If the energy resolution of the measurement is sufficient to resolve vibrational levels within a single electronic state of the molecular ion, then the spectrum will be sensitive to the vibrational composition of the excited state wavepacket through the FC factors (eqn (12)). If the electronic configuration of the excited state evolves, leading to a change in the electronic state of the ion populated by the probe laser pulse (*i.e.* complementary Koopmans' correlation), then this will be reflected in the electronic band structure of the TRPES. These concepts have already been introduced above and illustrated in Fig. 1; they are explored here in further detail.

2.4.1 Mapping vibrational wavepackets. Returning to the harmonic oscillator functions used in Section 2.2 for a prototype two-level system, we set $\Psi(R,t)$ as defined by eqn (7). The prepared wavepacket is therefore the same as that shown in Fig. 3. This wavepacket is purely vibrational and explores only a single potential energy surface, hence it evolves adiabatically. If we assume it is mapped onto a single electronic state of the ion *via* the probe pulse, then we can consider the resultant photoelectron signal in terms of FC factors alone. As in Section 2.2, the choice of harmonic oscillator functions is mathematically convenient but also provides a strong physical foundation—the same concepts hold for more complex vibrational and electronic wavepackets.

Fig. 4(a) shows $\langle\psi_{v+}(R)|\Psi(R,t=0)\rangle = \langle\psi_{v+}(R)|\psi_0(R)\rangle + \langle\psi_{v+}(R)|\psi_1(R)\rangle$ for three values of $\Delta R_e = R_e^+ - R_e$. In the case where the equilibrium bond length is unchanged upon ionization, $\Delta R_e = 0$, the only non-zero FC factors are for $\langle\psi_0(R)|\psi_0(R)\rangle$ and $\langle\psi_1(R)|\psi_1(R)\rangle$, as expected from the orthogonality of the Hermite polynomials. However, when the equilibrium bond-length is different in the final state, the FC

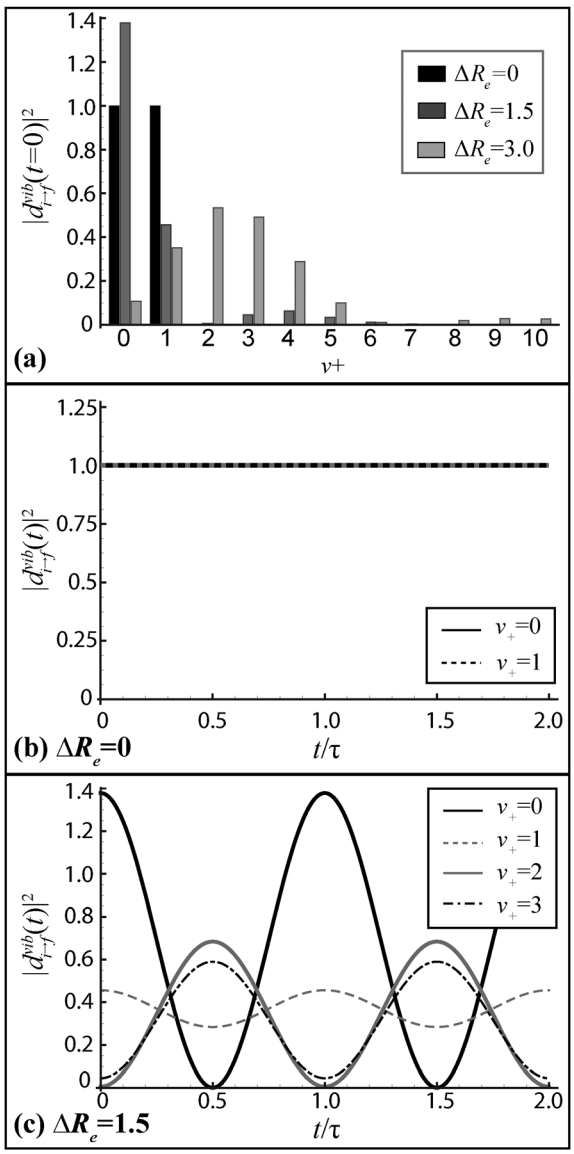

Fig. 4 (a) Vibrational overlap integrals $|\langle\psi_{v+}(R)|\Psi(R,t=0)\rangle|^2$ for various ΔR_e. As ΔR_e increases, a larger range of vibrational levels are populated in the ion. The two-level wavepacket $\Psi(R,t)$ is defined by eqn (7) and illustrated in Fig. 3(b). The time-dependent pump–probe signal, $|d_{i\to f}^{vib}(t)|^2$, is shown in panel (b) for $\Delta R_e = 0$ and (c) for $\Delta R_e = 1.5$. In the former case, no oscillations are observed as the wavepacket evolves. In the latter case, oscillations are observed for all v_+, although the exact form of these oscillations changes as a function of v_+.

factors to other v_+ levels are no longer zero. In this case, many vibrational levels are populated in the ion, hence a long vibrational progression will be observed in the spectrum.

Allowing for the time-dependence of the initial state provides a description of the time-dependent photoionization matrix element for this purely vibrational case:

$$\begin{aligned} d_{i\rightarrow f}^{vib}(t) &= \langle \psi_{v+}(R)|\Psi(R,t)\rangle \\ &= e^{-i\pi t}\langle \psi_{v+}(R)|\psi_0(R)\rangle + e^{-3i\pi t}\langle \psi_{v+}(R)|\psi_1(R)\rangle \end{aligned} \quad (13)$$

The value of $d_{i\rightarrow f}^{vib}(t)$ thus reflects the vibrational overlap integrals of the basis states modulated by the time-dependent phases. The observed photoelectron signal, as a function of photoelectron energy, E, and time, is then given by:

$$I(E;t) \propto |d_{i\rightarrow f}^{vib}(t)|^2 \quad (14)$$

The time-dependence of this signal, for different final vibrational levels v_+, is shown in Fig. 4(b) for $\Delta R_e = 0$ and Fig. 4(c) for $\Delta R_e = 1.5$, the simulated TRPES corresponding to this latter case is shown in Fig. 1(c). In the former case, no oscillations are observed in the signal. This is because the initial and final eigenstates are identical, so eqn (13) reduces to a single term with $v_+ = v$. The transitions shown in Fig. 4(b) are:

$$d_{i\rightarrow 0}^{vib}(t) = e^{-i\pi t}\langle \psi_0(R)|\psi_0(R)\rangle \quad (15)$$

$$d_{i\rightarrow 1}^{vib}(t) = e^{-3i\pi t}\langle \psi_1(R)|\psi_1(R)\rangle \quad (16)$$

Clearly, there are no terms involving both components of the prepared wavepacket in these transitions. Although time-dependent phase factors are still present in the matrix elements, the lack of interferences between different ionizing pathways means that these phases cannot be observed. This is made explicit from consideration of the modulus of the matrix elements given above:

$$|d_{i\rightarrow 0}^{vib}(t)|^2 = \langle \psi_0(R)|\psi_0(R)\rangle^2 = 1 \quad (17)$$

$$|d_{i\rightarrow 1}^{vib}(t)|^2 = \langle \psi_1(R)|\psi_1(R)\rangle^2 = 1 \quad (18)$$

Here, the observed signal is dependent upon only the (time-independent) FC factor, equal to unity in both cases.

In Fig. 4(c), where $\Delta R_e = 1.5$, oscillations are observed in the pump–probe signals, and the exact form of the oscillations is dependent on v_+. In this case the matrix elements to a single final state are as given by eqn (13), so interferences between the two components of the wavepacket are present, and will be mapped onto the observable.

A paradigmatic example of TRPES from a wavepacket on a single electronic state is the iodine experiment discussed in Section 3.2.1. Later work by the same group also explored the dependence of the signal on the probe wavelength, hence the final vibrational state.[64] A detailed computational exploration of final state effects can be found in ref. 65. Recent work has shown how TRPES data can be quantitatively analysed to provide highly detailed information on vibrational wavepackets and anharmonic couplings which give rise to IVR.[60]

2.4.2 Mapping non-adiabatic wavepackets. The next step in complexity is to consider a wavepacket which couples to another electronic state, allowing population of a second, vibrationally excited, electronic state through non-adiabatic couplings. This is illustrated in Fig. 2. In this model example, the pump pulse creates a wavepacket on electronic state α. As the wavepacket evolves it reaches the region of coupling between α and β, resulting in a splitting of the wavepacket, and population appears on β. In this case, labelling the electronic states α and β and assuming Koopmans' correlations to α_+ and β_+, respectively, we have:

$$\begin{aligned} d_{i\rightarrow f}(t) &= \sum_{\alpha,v_\alpha} A_{\alpha,v_\alpha}(t) e^{-i\left[E_{\alpha,v_\alpha}t/\hbar+\phi_{\alpha,v_\alpha}\right]}\langle \psi_{v_{\alpha+}}|\psi_{v_\alpha}\rangle \\ &\quad \times \langle \Phi_{\alpha+};\, \Psi_e|\hat{\boldsymbol{\mu}}\cdot\boldsymbol{E}_{probe}|\Phi_\alpha\rangle \\ &\quad + \sum_{\beta,v_\beta} A_{\beta,v_\beta}(t) e^{-i\left[E_{\beta,v_\beta}t/\hbar+\phi_{\beta,v_\beta}\right]}\langle \psi_{v_{\beta+}}|\psi_{v_\beta}\rangle \\ &\quad \times \langle \Phi_{\beta+};\, \Psi_e|\hat{\boldsymbol{\mu}}\cdot\boldsymbol{E}_{probe}|\Phi_\beta\rangle \end{aligned} \quad (19)$$

Here the A_n coefficients are again time-dependent because the composition of the wavepacket, in terms of the B–O states, changes as the wavepacket explores the potential surface and population is transferred from α to β. The presence of time-dependent coefficients in the excited state wavepacket leads to more complex behaviour than the purely vibrational case. Here we expect to see changes in the band (energy) structure of the photoelectron spectrum as a function of time, for example the appearance of low energy features at later Δt in the case illustrated in Fig. 2; this is in contrast to the periodic oscillations of a set of vibrational bands, as observed for the purely vibrational case. A prototypical example of mapping a vibronic wavepacket is the TRPES of decatetraene discussed in Section 3.2.2.

2.5 TRPADs

In the preceding discussion, the form of the photoelectron wavefunction, Ψ_e, has not been discussed. Often, in analysis of TRPES measurements, the electronic matrix element involving Ψ_e can be treated purely as a weighting factor without any loss in the utility of a TRPES measurement. However, this implicitly assumes that the ionization matrix element is photoelectron energy independent. In reality, Ψ_e is a complex wavefunction, with energy and angular momentum dependence, and is a key element in understanding photoelectron angular distributions (PADs). Although this complexity is difficult to account for in both *ab initio* studies and analysis of experimental results, it can be used for our advantage in order to provide more information on the excited state dynamics than can be obtained from TRPES alone, particularly in the case of corresponding ionization correlations. Here we first consider the most general form for PADs and the symmetry requirements for photoionization, providing a qualitative framework, can be readily brought to bear to interpret experimental data. We then explore a quantitative model for PADs which provides deeper insight into the role of Ψ_e, and finally provide a model example of time-resolved PADs.

2.5.1 General form of photoelectron angular distributions. The most general expression for angular correlations in scattering was given by Yang,[66] based upon symmetry arguments.

This general form for the angle-resolved flux can be written[27]

$$I(\theta,\phi) = \sum_{L=0}^{L_{max}} \sum_{M=-L}^{L} \beta_{LM} Y_{LM}(\theta,\phi) \qquad (20)$$

where the Y_{LM} are spherical harmonic functions and the β_{LM} are the expansion parameters, often termed *anisotropy parameters*; L is the rank of the spherical harmonic (or multipole moment) and M the order of the spherical harmonic. Eqn (20) is always applicable, but the allowed values of L and M depend on angular momentum and symmetry restrictions which, in turn, depend on both the properties of the molecule under study and the experimental geometry.

For example, for the case of photoionization referenced to the lab frame (LF), L_{max} corresponds to twice the number of photons which interact with the system; this interaction determines the maximum anisotropy that can be created in the LF from an initially isotropic sample.[27,61] If reflection symmetry is present, L must be even, and cylindrical symmetry (no ϕ dependence) restricts terms to $M = 0$ only. In the common case of a 1-photon pump, 1-photon probe experiment where the polarization vectors are parallel, this is indeed the case, and therefore only terms with $L = 0,2,4$ and $M = 0$ are allowed. Because $Y_{L,0} \propto P_L(\cos\theta)$, where $P_L(\cos\theta)$ are Legendre polynomials in $\cos\theta$, eqn (20) is often rewritten for this common case as‡‡:

$$I(\theta) = \sum_{L=0}^{L_{max}} \beta_L P_L(\cos\theta) \qquad (21)$$

If, however, the polarization of the probe laser is rotated relative to that of the pump laser, the cylindrical symmetry is broken and terms with $M \neq 0$ can be present in the LF.[67] For further discussion of the general form of the PAD in other cases, see ref. 27.

In the molecular frame (MF) the allowed terms in eqn (20) are not determined by the experimental geometry, but rather by molecular symmetry and the maximum angular momentum component of the photoelectron wavefunction.[27,68] These considerations are discussed further in the following sections, but in general it can be concluded that MF measurements display much richer structure than LF measurements and are hence desirable in order to maximize the information gained from experiment.[27,33,69]

Most generally, eqn (20) provides a functional form with which experimental data can be fitted. However, more detailed understanding of the PADs requires the derivation of the β_{LM} in terms of the ionization matrix elements, *i.e.* we need to understand how the general angular expansion given by eqn (20) relates to

$$I(\theta,\phi) = d^*_{i\to f} d_{i\to f} \qquad (22)$$

where coherences between different angular momentum components are present.

‡‡ It is important to note when comparing distributions of the form of eqn (21) to those expressed in spherical harmonics (eqn (20)) that the $\beta_L \neq \beta_{LM}$ because the angular functions have different normalization factors.

2.5.2 Symmetry considerations. The determination of which matrix elements are allowed (non-vanishing) can be made purely from symmetry arguments. This is useful because changes in the symmetry of Ψ_e are directly reflected in the TRPADs, so interpretation of experimental results can be made at this level without the significant effort of more quantitative treatments.

For the dipole matrix element to be non-zero, the direct product of the initial state, final state and dipole operator symmetries, denoted by Γ_i, Γ_f and Γ_{dipole}, respectively, must contain the totally symmetric representation of the molecular symmetry (MS) group (isomorphic to the point group in rigid molecules), denoted Γ^s.[40] For the specific case of photoionization, the final state can be split into the symmetry species of the ion and the photoelectron:[70]

$$\Gamma_e \otimes \Gamma_f \otimes \Gamma_{dipole} \otimes \Gamma_i \supset \Gamma^s \qquad (23)$$

In general Γ_i and Γ_f denote the symmetry of the full vibronic wavefunction, although electronic and vibrational symmetry components may be further separated by application of the FC principle to give:

$$\Gamma_{v_{\alpha+}} \otimes \Gamma_{v_\alpha} \supset \Gamma^s \qquad (24)$$

$$\Gamma_e \otimes \Gamma_{\alpha+} \otimes \Gamma_{dipole} \otimes \Gamma_\alpha \supset \Gamma^s \qquad (25)$$

For photoionization, an interesting possibility arising from the second condition is that a change in Γ_α—*i.e.* a change in electronic symmetry of the excited state—implies a change in Γ_e and/or $\Gamma_{\alpha+}$ in order that ionization remains allowed. In the case of corresponding ionization correlations, there is no change in $\Gamma_{\alpha+}$, hence there must be a change in the symmetry of the photoelectron wavefunction. As discussed below, the TRPAD is highly sensitive to the form of Ψ_e, so a change in symmetry may lead to a significant change in the observable PAD. Observation of TRPADs, at a given photoelectron energy, can therefore be considered as a phenomenological indication of changes in the electronic character of $\Psi_i(t)$.§§ One example of the utility of a symmetry-based analysis is the $(NO)_2$ study discussed in Section 3.2.3; see, for instance, ref. 71 and 72 for more recent examples of symmetry-based analysis.

2.5.3 Partial wave expansion. The continuum wavefunction can be expanded in terms of *partial waves*, ψ_{lm}, which in turn are decomposed into radial and angular parts.[73,74] We follow the notation and phase convention of ref. 75:

$$\Psi_e(\boldsymbol{k}) = \sum_{l,m} \psi_{lm}(\boldsymbol{k}) = \sum_{l,m} A_{lm} \chi_{kl}(r) Y_{lm}(\hat{\boldsymbol{r}}) \qquad (26)$$

$$A_{lm} = 4\pi i^l e^{-i\eta_{lm}} Y^*_{lm}(\hat{\boldsymbol{k}}) \qquad (27)$$

§§ We note here that care should be taken to distinguish the effect of such electronic non-adiabatic dynamics on TRPADs from rotational effects causing changes in the molecular axis alignment as a function of time. These can usually be distinguished by their timescale—typically picosecond for rotational motion—or removed by recording TRPADs in the molecular frame. As already discussed in Section 2.1, rotations are separable provided there are no couplings between rotations and other degrees of freedom. For further discussion on these points see, for example, ref. 33, 41 and 42.

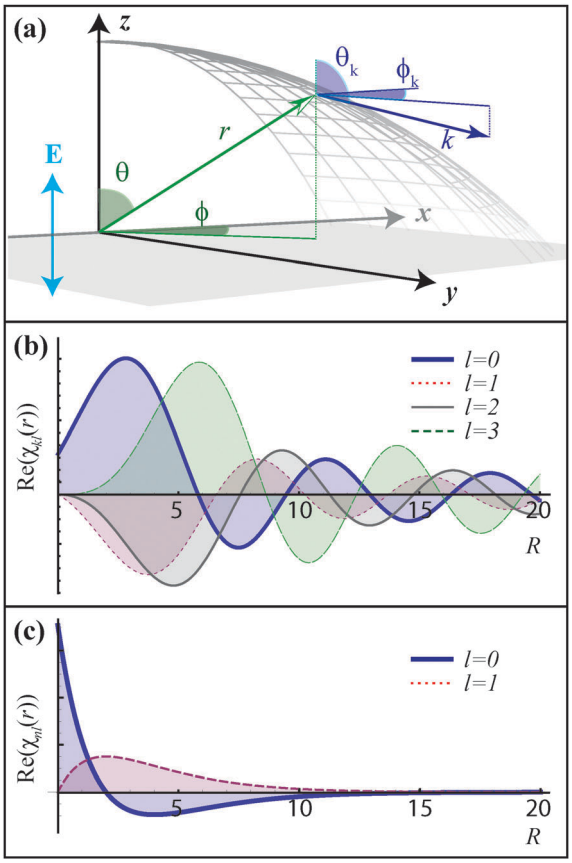

Fig. 5 (a) Coordinate frame definitions for angle-resolved photoionization, showing position vector $\boldsymbol{r}$ and momentum vector $\boldsymbol{k}$. (b) Coulomb radial wavefunctions for $l = 0$–3, $k = 1$ a.u. plots show the real part of the wavefunction. For larger l the peak of the wavefunctions move to larger r, this is the effect of the (l-dependent) centrifugal barrier. (c) Hydrogenic wavefunctions for $n = 2$, $l = 0,1$.

Here we work in a spherical coordinate system (see Fig. 5(a)), with position vector $\boldsymbol{r} = (r,\theta,\phi)$ and momentum vector $\boldsymbol{k} = (k,\theta_k,\phi_k)$. The z-axis is chosen to coincide with the incident radiation polarization vector $\boldsymbol{E}$. $\chi_{kl}(r)$ is the radial wavefunction, expressed as a function of position r for a given photoelectron wavenumber k and orbital angular momentum l; Y_{lm} are spherical harmonics describing the angular wavefunction in the directions defined by the unit vectors $\hat{\boldsymbol{r}}$ and $\hat{\boldsymbol{k}}$; η_{lm} is the phase (often called the *scattering phase*) and the quantum numbers l, m label the orbital angular momentum and its projection onto the z-axis. Often l, m are labelled as per atomic orbitals, with $l = 0, 1, 2, \ldots$ denoted s, p, d, …, and $m = 0, 1, 2, \ldots$ labelled σ, π, δ, …. Finally, we note that in the atomic case there is no distinction between the lab and atomic frame, so we can choose z to be coincident with the laser polarization vector $\boldsymbol{E}$. For molecules, we can work in the molecular (or body-fixed) frame and choose the z-axis to be the highest symmetry axis. Frame rotations are then required to express wavefunctions in the lab (or space-fixed) frame defined by $\boldsymbol{E}$.[33,41,68]

For a Coulombic potential, the $\chi_{kl}(r)$ have exact solutions,[73] which asymptotically match the sinusoidal free-electron wavefunction, with phases given by the Coulomb phase. An example of the radial wavefunctions is shown in Fig. 5(b), plotted for $k = 1$ atomic unit (a.u.). Of particular note is the form of the radial wavefunctions at small r: as l increases, the amplitude at small r decreases. This behaviour is due to the l dependence of the effective potential energy surface, which gives rise to a *centrifugal barrier*. This barrier pushes high l continuum states to large r, thus preventing coupling of bound and high l continuum waves. The centrifugal barrier is often invoked to explain the dominance of low l waves in the continuum wavefunction, with $l \leq 4$ typically expected in photoionization.[27,76]

2.5.4 Quantitative treatment of TRPADs. Cooper and Zare first showed how using the partial wave expansion in the electronic part of the photoionization matrix elements allows for a separation of the radial and angular wavefunctions.[75,77] Here we illustrate the Cooper and Zare solution for a one-electron system in order to give insight into PADs, then generalize for the molecular and time-dependent cases.

For a one-electron atom, the ionization matrix element is purely electronic and can be written as:

$$d_{i\to f}^{atm} = \langle \Psi_f | \hat{\boldsymbol{\mu}}\cdot\boldsymbol{E} | \Psi_i \rangle \equiv \langle \Psi_e | \hat{\boldsymbol{\mu}}\cdot\boldsymbol{E} | \Psi_i \rangle \tag{28}$$

Using hydrogenic bound states and expanding the dipole operator as $\hat{\boldsymbol{\mu}}\cdot\boldsymbol{E} \propto rY_{1,0}(\theta,\phi)$ for light linearly polarized along the z-axis allows the matrix elements to be expanded in radial and angular components:

$$\langle \Psi_e | rY_{10}(\hat{\boldsymbol{r}}) | \Psi_i \rangle = \sum_{l,m} A_{lm}^{*} \langle Y_{lm}(\theta,\phi) | Y_{10}(\theta,\phi) | Y_{l'm'}(\theta,\phi) \rangle \times \langle \chi_{kl}(r) | r | \chi_{nl'}(r) \rangle \tag{29}$$

Here the primed terms are quantum numbers for the initial state, and unprimed terms for the final state; n is the principal quantum number for the bound state.

The radial integral $\langle \chi_{kl}(r) | r | \chi_{nl'}(r) \rangle$ must be solved numerically or obtained from experiment. The angular part has analytic solutions:[77,78]

$$\langle Y_{lm}(\theta,\phi) | Y_{10}(\theta,\phi) | Y_{l'm'}(\theta,\phi) \rangle = (-1)^{l-m+(l'-l+1)/2} l_{>}^{1/2} \times \begin{pmatrix} l & 1 & l' \\ -m & 0 & m' \end{pmatrix} \tag{30}$$

where the final term in brackets is a Wigner 3j symbol which defines the angular momentum coupling,[78,79] and in this case encodes the well-known atomic angular momentum selection rule for linearly polarized light along the z-axis, $l = l' \pm 1$ and $m = m'$. The notation $l_>$ denotes the greater of l or l'.

The observable photoelectron flux as a function of angle, $I(\theta,\phi) = d_{i\to f}^{atm} d_{i\to f}^{atm*}$, can now be found in terms of these radial and angular terms:

$$I(\theta,\phi) = \frac{1}{2l'+1} \sum_{m'} \sum_{l_1,m_1} \sum_{l_2,m_2} A_{l_1m_1} A_{l_2m_2}^{*} r_{kl_1nl'} r_{kl_2nl'}^{*} \gamma_{l_1m_1l_2m_2l'm'} \tag{31}$$

Here all the angular momentum coupling terms arising from the coherent square of eqn (30) are collected into $\gamma_{l_1 m_1 l_2 m_2 l' m'}$, and $r_{kln'}$ are the radial integrals. An (incoherent) summation over initial levels m' is made assuming equal population of all m', leading to the degeneracy prefactor. In this form the structure of the PAD is emphasized: each partial wave channel is weighted according to the radial and angular momentum overlap integrals and, due to the coherent squaring of $d_{i\to f}^{atm}$, the summation contains terms in $l = \{l_1,l_2\}$, where diagonal terms have $l_1 = l_2$ and off-diagonal terms have $l_1 \neq l_2$. The parameters A_{lm} contain the scattering phases. From this, the PAD can be recognized as an angular interference pattern arising from *interferences between the different partial waves*.

Interferences in the PAD originate from the l-dependent scattering phases, with amplitudes determined by angular momentum coupling and the radial overlap integrals between the initial and final states. Hence, the electronic structure of the initial state, final state and the photoelectron energy all play important roles in the form of the PAD. As an aid to visualizing such angular interference patterns, Fig. 6 shows an example for an s and d partial wave in the case where all other parameters are set to unity, hence $d_{i\to f}^{atm} \propto Y_{00} + Y_{20}e^{-i\eta_{20}}$. In the case where the partial waves are in phase ($\eta_{20} = 0$) there is constructive interference at the poles of the distribution, and destructive interference around the equator, leading to a distribution which looks like a p_z function. The opposite situation occurs at $\eta_{20} = \pi$, yielding a more complex form in the xy plane. This example demonstrates the sensitivity of the PAD to the relative phases of the partial waves and highlights their non-intuitive nature: even in this simple case, the linear combination of just two partial waves leads to a range of possible angular distributions.

Although eqn (31) has been derived for a one electron system for simplicity, the general form of the equations describing the PAD for more complex cases—multi-electron atoms or molecules—is very similar and can be interpreted in the same way, particularly under the FC approximation whereby the radial matrix elements remain purely electronic in composition. The complexity, however, is increased considerably because the potential for a multi-electron atom or molecule is not a centrally symmetric Coulombic potential as in the one-electron atomic case above. The potential will, in general, contain multi-polar contributions from short range electron–electron interactions and from the structure of the molecule. The net result is an increase in the complexity of both the bound orbital and free electron wavefunctions. However, because the multi-polar terms of the potential fall off more rapidly with r than the Coulombic contribution, the problem can be considered in terms of a short range (non-Coulombic) region and a long range (Coulombic) region. Under this separation, the partial wave description of Ψ_e remains good in the asymptotic limit ($r \to \infty$), and the scattering phases η_{lm} carry information on the short range scattering, although *ab initio* calculation of these scattering phases remains a challenging problem. For more detailed discussion of the molecular case, see for example ref. 27, 68 and 76, also ref. 80 which presents quantitative model calculations for the molecular case.

For a time-dependent initial state, the TRPAD will be sensitive to the evolving state through the dependence of the ionization matrix elements on this state. Under the FC approximation (eqn (11)), the PAD is *directly related* to the electronic structure of the initial and final states of the system, Φ_α and $\Phi_{\alpha+}$. For example, in a case where α is initially prepared and a second electronic state β is populated over time, the PAD will change to reflect the evolving electronic character of the system. This is the utility of the TRPAD, and is particularly important in cases of corresponding ionization correlations where changes in the TRPES may not directly reveal the evolution of the electronic character of the excited state.

2.5.5 Mapping evolving electronic character with TRPADs. To provide further insight into the changes that could be expected in a TRPAD, we present a model example loosely based on the $(NO)_2$ experiments discussed in Section 3.2.3. We consider here a one-electron case where an s orbital is initially populated and exponentially decays to a p_z state over time. Assuming these states are iso-energetic and neglecting any relative phase of the electronic states, this decay can be modelled as a time-dependence of the $A_n(t)$ parameters in eqn (7):

$$|\Psi(t)\rangle = A_s(t)|\Phi_s\rangle + A_p(t)|\Phi_p\rangle \quad (32)$$

$$A_s(t) = e^{-t/\tau} \quad (33)$$

$$A_p(t) = 1 - e^{-t/\tau} = 1 - A_s(t) \quad (34)$$

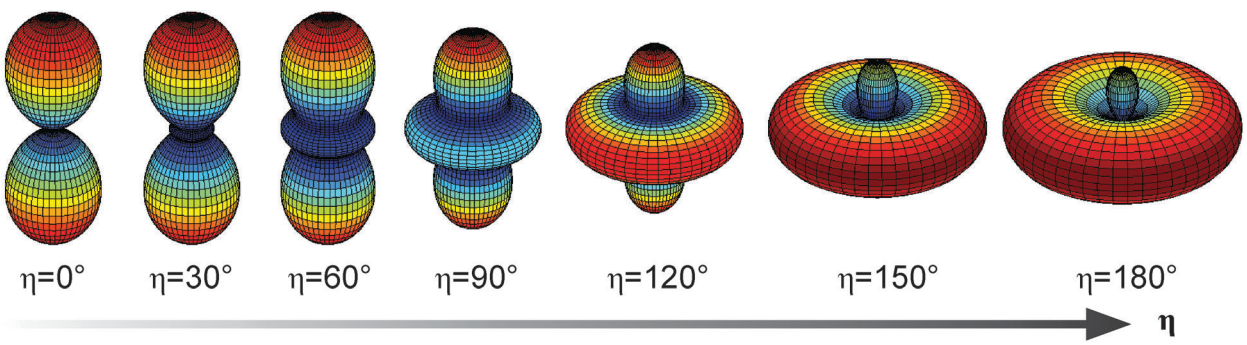

Fig. 6 Illustration of the effect of phase on PADs, see Section 2.5.4 for details. PADs are plotted in spherical polar form. As the phase η_{20} is varied, the interference of terms Y_{00} and Y_{20} is affected, leading to different angular interference patterns.

where τ is the lifetime of the initially prepared state. The dipole matrix elements are therefore now time dependent, and can be written as the sum of the two components of $\Psi(t)$:

$$d_{i\to f}^{atm} = A_s(t)\langle \Psi_e^s|\hat{\boldsymbol{\mu}}\cdot\boldsymbol{E}|\Phi_s\rangle + A_p(t)\langle \Psi_e^p|\hat{\boldsymbol{\mu}}\cdot\boldsymbol{E}|\Phi_p\rangle \quad (35)$$

where the superscript on Ψ_e is introduced to label the photoelectron wavefunction as correlating with the s or p bound state. This can further be expanded in terms of the allowed partial wave components of the free electron, ψ_l, as defined by the selection rule $\Delta l = \pm 1$:

$$d_{i\to f}^{atm} = A_s(t)\langle \psi_p(\boldsymbol{k})|\hat{\boldsymbol{\mu}}\cdot\boldsymbol{E}|\Phi_s\rangle + A_p(t)(\langle \psi_s(\boldsymbol{k})|\hat{\boldsymbol{\mu}}\cdot\boldsymbol{E}|\Phi_p\rangle + \langle \psi_d(\boldsymbol{k})|\hat{\boldsymbol{\mu}}\cdot\boldsymbol{E}|\Phi_p\rangle) \quad (36)$$

The matrix elements appearing here have already been given in terms of radial and geometric parts by eqn (29). We assume that the bound states are hydrogenic and the continuum radial wavefunctions are Coulomb waves (as shown in Fig. 5(b) and (c)), and solve the radial integrals numerically. Eqn (30) is used to provide the geometric part of the solution. The results of this calculation for $k = 1$ a.u., namely the ionization cross-sections for each partial wave channel and the TRPADs, are shown in Fig. 7, along with the population dynamics. The total cross-section is defined, as in eqn (14), by $|d_{i\to f}^{atm}|^2$; the partial wave cross-sections are given by the square of each partial wave component, for example $|d_{s\to p}^{atm}|^2 = |A_s(t)\langle \psi_s(\boldsymbol{k})|\hat{\boldsymbol{\mu}}\cdot\boldsymbol{E}|\Phi_p\rangle|^2$ gives the p-wave cross-section.

At $t = 0$ the bound state is purely s in character, and photoionization couples only to a continuum p-wave. The ionization cross-section thus contains only a p-wave contribution, and the PAD resembles a p-wave due to the absence of interferences. As population is transferred from $\Phi_s \to \Phi_p$ ionization to s and d continuum waves becomes possible. At $t = 0.2\tau$ the ionization cross-section contains small contributions from these additional components. The total cross-section is increased relative to $t = 0$, and the PAD has changed significantly. In this example, the addition of small s and d-wave contributions to the dominant p wave pushes out the waist, and narrows the lobes of the PAD. This sensitivity is due to the nature of the PAD as an interference phenomenon, consequently it is sensitive to even small contributions from the partial waves.

As the excited state population continues to evolve with time, so the PAD continues to evolve, tracking the electronic character of the excited state. In this case, the ionization cross-sections to the s and d continua rapidly grow, and dominate by $t = \tau$. This is reflected in the PAD which looks increasingly d-like. However, as at other t there is also a significant s contribution with different phases from the d-wave. This influences the final form of the PAD, as indicated in Fig. 6. If additional phase contributions played a role, such as an additional non-Coulombic scattering phase shift, then the shape of the PAD would change as a consequence.

It is insightful to compare these observations to the TRPES. In this case of corresponding Koopmans' correlations, the TRPES reflects the total ionization cross-section and shows a gradual rise in the ionization cross-section as a function of time. This behaviour is shown by the grey dotted line in Fig. 7(b); similar lineshapes are seen for the decay of the

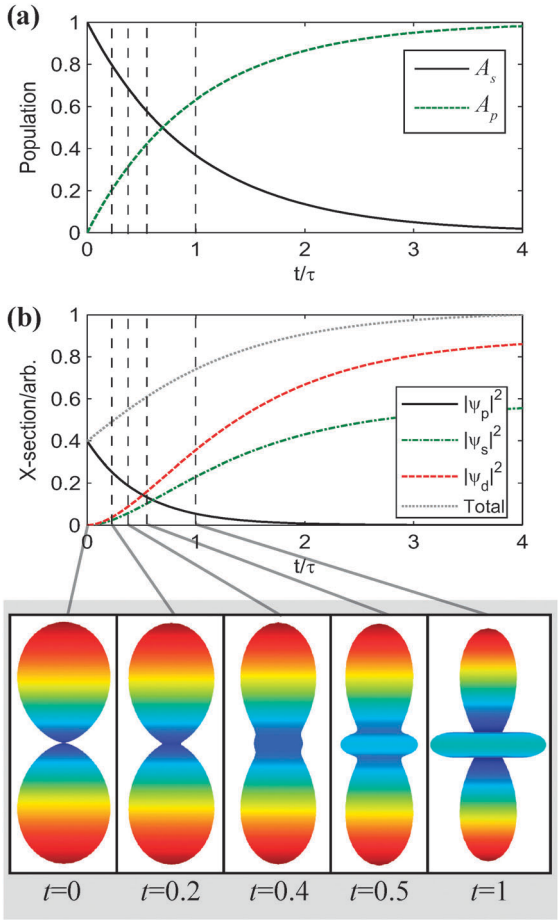

Fig. 7 Quantitative modelling of TRPADs for a two-level system, see Section 2.5.5 for details. (a) Excited state populations $A_s(t)$ and $A_p(t)$. (b) Photoionization cross-sections, shown for each partial wave channel and total (l-summed) cross-section. (c) Polar plots showing the TRPADs for the two-state model system.

intermediate state and rise of the final product in the experimental TRPES for $(NO)_2$ shown in Fig. 13 (although, in that case, a more involved three-state kinetic model is required to explain the observations). Changes in the TRPES by definition provide evidence for time-dependence of the excited state, in this example showing a rise in photoelectron yield as population is transferred from $\Phi_s \to \Phi_p$. The nature of the excited state, and therefore the continuum state populated upon ionization, plays a role in the TRPES through the cross-sections and phases of the partial waves. For example, at $t = 4\tau$ the total cross-section is less than the (incoherent) sum of the s and d-wave partial cross-sections. This is due to partially destructive interference between ψ_s and ψ_d. However, from the TRPES alone, it is difficult, if not impossible, to gain clues as to the detailed nature of the excited state evolution. The TRPAD, in this example, changes from a p-like form to a d-like form. With knowledge of the selection rules from the excited state, TRPADs obtained experimentally could thus be analysed to reveal directly the $\Phi_s \to \Phi_p$ nature of the population transfer, mapping the electronic population dynamics.

In the example presented here, a simple atomic-like model system has been considered. More generally, we are interested

in the photoionization dynamics of polyatomic molecules. As detailed above, an analogous treatment can be followed, but with many partial waves required to describe the continuum. In this case the TRPAD can still be considered as a map of the electronic evolution of the excited state, but this mapping is naturally more complex and determination of the excited state character less straightforward. The $(NO)_2$ example given in Section 3.2.3 shows how symmetry arguments can be invoked to understand the TRPAD in a more complicated case; a more recent example is given by studies on CS_2.[69,71] Both examples highlight how the TRPAD is complementary to the TRPES in determination of excited state dynamics.

2.6 Summary

In this section we discussed some general background theory for time-resolved photoelectron measurements, and illustrated these points with simple model systems. In particular we stressed the role of time-resolved photoionization as the projection of a time-dependent wavepacket onto a set of final states, and how measurement of the photoelectron energy spectrum and angular distribution provides observables which are sensitive to different aspects of the wavepacket motion. In the following section, we highlight recent experimental examples which provide prototypical examples of the underlying concepts.

3 Experimental methods and applications

In this section, we will start with a very brief introduction to different experimental methods applied to TRPES measurements, followed by applications of TRPES to studies of excited state molecular dynamics.

3.1 Experimental methods used in TRPES measurements

There are many different experimental methods used in TRPES studies: zero-kinetic energy (ZEKE) photoelectron spectroscopy,[81–83] magnetic bottle time-of-flight spectroscopy (MAGBOTT),[84,85] velocity-mapped electron imaging (VMI),[31,86,87] coincidence imaging spectroscopy (CIS),[88,89] and photoelectron–photoion coincidence spectroscopy (PEPICO).[22,90] They vary in complexity and information content. The selection of experimental technique(s) is dependent on the problems of interest. In the following, a very brief introduction to these experimental techniques is given in order to provide enough background to follow the experimental examples presented in Section 3.2. The emphasis is on the level of differential measurement of which each technique is capable. We refer interested readers to the corresponding references for further details.

ZEKE was originally invented for very high resolution photoelectron spectroscopy. In traditional photoelectron spectroscopy, atoms or molecules are ionized by one or more photons with total energy greater than the ionization energy of the sample. Energetic electrons are generated and detected. The kinetic energy distribution of the electrons provides information on the internal states of an ion. The standard resolution limit on determining photoelectron kinetic energies is typically about 10 meV (80 cm^{-1}). In ZEKE measurements, the total photon energy matches exactly the energy difference between an ionic molecular state and a neutral state. Photoabsorption leads to the preparation of very high-n Rydberg states which are subsequently pulsed-field ionized[83] using a low voltage electric pulse. By tuning the wavelength of a narrow bandwidth laser, different internal states of the ion are reached and the ionization energies are measured. In this way, a huge improvement in spectral resolution is achieved, with $\ll 1$ cm^{-1} being possible.[83] Besides very high spectral resolution, ZEKE has the advantage of being insensitive to background (*i.e.* kinetic) electrons produced by other ionization channels. ZEKE spectroscopy has also been combined with picosecond[91] and femtosecond[20,64,92] pump–probe techniques to study vibrational wavepacket dynamics. In such situations, the choice of ZEKE as the detection scheme is not because of its high energy resolution, but for state selection of the ion. In ps or fs ZEKE measurements, only transitions to ionic states which are within the bandwidth of the probe pulse are detected. In contrast, in an energy-integrated photoionization measurements (ion yield or total electron signal), all ionic states which are energetically accessible can be populated according to their individual transition probabilities (*e.g.* FC factors). The signal is therefore an incoherent weighted sum of transitions to all open channels. In general, this leads to loss of information due to the averaging over ionization channels to different ionic states. In Section 3.2.1, the vibrational wavepacket dynamics of an I_2 molecule[20,64] is given as an illustration on how the fs time-resolved ZEKE measurement is used to study vibrational wavepacket dynamics on a single potential surface.

The principle of all photoelectron techniques other than ZEKE is similar: the kinetic energy distribution of photoelectrons is obtained by recording their time-of-flight (TOF) and/or positions at a 2D detector. From the kinetic energy distribution of the electrons, the corresponding internal states of the ion are determined by energy conservation. The magnetic bottle technique is able to measure the kinetic energy distribution of the photoelectrons. VMI is able to measure both the energy and angular distribution of the photoelectrons. PEPICO is used to measure the TOF of both photoelectrons and photoions coincidently; the TOF of the latter provides the information on the charge-to-mass ratio of the cation correlated with the photoelectron. This information is necessary in the study of the dynamics of atomic or molecular clusters, or photofragmentation dynamics of molecules or clusters. CIS measures the full 3D distributions of both photoelectrons and photoions coincidently, as shown in Fig. 8. The femtosecond pump and probe laser beams are crossed with a molecular beam in the horizontal plane. The pump pulse prepares an excited state wavepacket of the molecule which subsequently evolves on the excited state potential energy surface. A time-delayed probe pulse ionizes the excited state molecules, or the reaction intermediates, or reaction products. The generated photoelectron is accelerated in the vertical direction and towards a time- and position-sensitive detector,[93–95] while the ion is accelerated in the opposite direction towards another detector. Both TOF and position of the particle on the detector are recorded. The TOF gives the velocity of the particle in one dimension and the position gives the other two dimensions of the particle velocity. The arrival time of the ion also provides mass information. The signal level is kept low enough to make sure that only the photoelectron and photoion originating from the same ionization

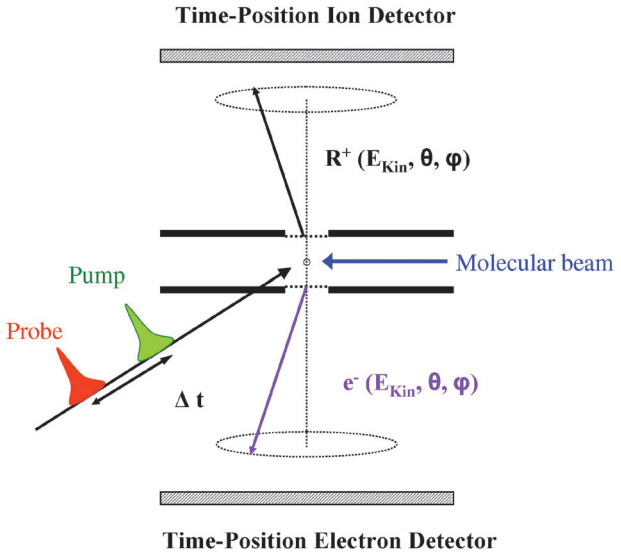

Fig. 8 Schematic diagram of the femtosecond time-resolved coincidence imaging spectrometer. A detailed description is given in the text.

event are recorded. This leads to 6D fully correlated imaging. In cases where the parent molecule dissociates after photoionization and the fragments recoil along the direction of the breaking bond, the recoil direction of photofragment provides orientation information of the parent molecule at the moment of ionization (the axial recoil approximation). Therefore, time-resolved coincidence imaging spectroscopy (TRCIS) measurements, which fully correlate photofragment and photoelectron recoil distributions as a function of time, permit dynamical observations from the molecule's point of view in favorable cases.[88,96]

3.2 Applications of TRPES to molecular dynamics

In this subsection, the application of TRPES to studies of molecular dynamics will be illustrated by three experimental examples: simple vibrational wavepacket dynamics on a single potential energy surface; disentangling electronic from vibrational dynamics *via* time- and energy-resolved photoelectron spectra measurements; identifying the electronic character of the intermediate state involved in a non-adiabatic process using TRPADs measured in the molecular frame.

3.2.1 Vibrational dynamics on a single potential energy surface. As outlined in Section 2.4.1, one of the simplest applications of TRPES is the study of bound wavepacket motion on a single potential energy surface. Here, we will show the example of wavepacket dynamics in the B electronic state of molecular iodine using fs ZEKE spectroscopy. Further details of these experiments can be found in ref. 20 and 64.

In the experiment, a pump laser of 580 nm and 95 fs pulse duration excited I_2 molecules to vibrational levels $v' = 14$–17 within the B electronic state. The probe pulse was tuned between 300–350 nm and had a pulse duration of 100 fs. This allowed tuning of the (two-photon) probe energy from below the ionization potential (IP) to high vibrational levels of the ground state of the ion. In Fig. 9, fs pump–probe scans of I_2 (B) state wavepacket dynamics using ZEKE detection are shown. The wavelength of the probe laser was 345 nm for projection onto $v^+ = 0$–1 in the ion. A modulation period of

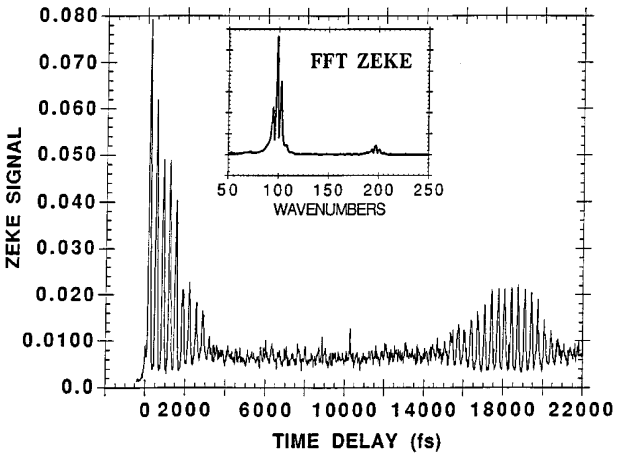

Fig. 9 Pump–probe ZEKE scans of the 580 nm I_2 (B) wave-packet dynamics using 345 nm probe (final state, $v^+ = 0$, 1) showing 340 fs modulation. Dephasing and recurrence of the wave packet are seen. The Fourier transform power spectra, inset, show that coherences between vibrational levels $v' = 14$–15, 15–16, 16–17 are involved. Reprinted with permission from ref. 20. Copyright [1995], American Institute of Physics.

340 fs was observed, corresponding to the average vibrational frequency of I_2 (B, $v = 14$–17) that is excited by the 580 nm pump pulse. The modulation is due to the interferences between transitions from a set of vibrational levels in the B state to a final state of the ion, as discussed in Section 2.4.1. Due to the anharmonicity of the potential energy curve of the B state, the spacings between two consecutive levels decrease slightly with the increase of the vibrational quantum number. Therefore, the modulations from different sets of vibrational levels are not exactly in phase and will gradually become out of phase (dephasing), which is seen in Fig. 9: the total modulation decays after about ten vibrational periods. The I_2 (B) state excited at 580 nm is a bound state and therefore the dephased wave packet must rephase, as shown in Fig. 9, beginning around 15 ps. The inset in Fig. 9 is the Fourier transform power spectra (FFT) of data set. The three large peaks in the FFT near 100 cm^{-1} correspond to nearest-neighbor coherences between vibrational levels $v = 14$–15, 15–16, 16–17 in the B state. A slight contribution at the second harmonic (near 200 cm^{-1}) is due to next-nearest-neighbor coherences.

3.2.2 Disentangling electronic from vibrational dynamics using TRPES. In the last subsection, we discussed how the TRPES technique provides details of vibrational dynamics in simple molecules on a single potential surface. As discussed in Section 2.3, time-resolved photoelectron spectroscopy is also applicable to studies of ultrafast non-adiabatic processes[90,97,98] and spin–orbit coupling[99] in isolated polyatomic molecules. In polyatomic molecules, excitation to electronically excited states often results in the rapid mixing of vibrational and electronic motions which induces both charge redistribution and energy flow in the molecule.[6,100] Disentangling electronic from vibrational motions is critical in studies of non-adiabatic processes. In the following, the study of ultrafast internal conversion in all-*trans* 2,4,6,8 decatetraene (DT, $C_{10}H_{14}$) will be given as an example of disentangling electronic from vibrational dynamics

using TRPES measurements. Detailed information of these experiments can be found in ref. 48 and 101 and references therein.

The molecular orbitals which are important in the internal conversion of DT (IP = 7.3 eV) are shown in Fig. 10. The S_0 (1^1A_g) electronic ground state is a single configuration. The first optically allowed transition (~4.3 eV) is to the second excited state, S_2 (1^1B_u), which is predominantly a singly excited configuration. The lowest excited state (~3.6 eV), however, is the dipole forbidden S_1 (2^1A_g) state which arises from configuration interaction between singly and doubly excited A_g configurations. Non-adiabatic coupling, leading to ultrafast internal conversion from S_2 to S_1, is promoted by vibrational motions of b_u symmetry. The most probable electronic configurations of the cation expected upon removal of the highest-lying electron from the neutral excited state are indicated in Fig. 10 by dashed arrows. The S_2 excited state correlates with the D_0 (1^2B_g) ground state of the cation. The S_1 state, by contrast, mainly correlates with the D_1 (1^2A_u) first excited ionic state. Therefore, a band switching in the time-resolved photoelectron spectrum is expected to occur during the internal conversion.

Fig. 11(a) shows the energy level scheme relevant to the experiment. A femtosecond pump pulse at 287 nm prepared the excited S_2 state at its electronic origin. The system then evolves into a vibrationally hot (0.7 eV) S_1 electronic state. The evolving wavepacket is monitored by photoionization into the ground and first excited electronic states of the cation with a fs, UV probe pulse at 235 nm.

The time-resolved experimental photoelectron spectra (Fig. 11(b)) show a shift of electrons from an energetic band

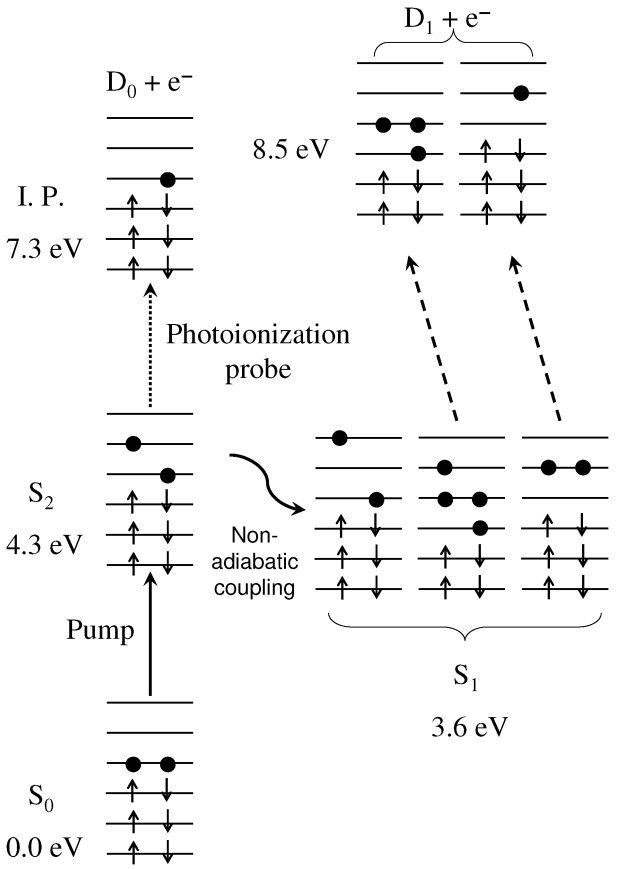

Fig. 10 Molecular orbital configurations and photoionization correlations in all-*trans* 2,4,6,8 decatetraene, DT. The optically coupled S_2 (excitation at 4.3 eV shown by straight solid arrow) state is a singly excited configuration, whereas the lower-lying optically forbidden S_1 (3.6 eV) state is composed of both singly and doubly excited configurations. The curved solid arrow indicates non-adiabatic coupling in the excited state. On removal of the highest-lying electron, S_2 correlates with the D_0 cation ground-state configuration with an ionization potential of 7.3 eV, whereas S_1 correlates predominantly with the D_1 cation excited-state configurations at 8.5 eV. It is therefore expected, assuming a single active electron, that the photoionization electronic channel should switch from $D_0 + e^-$ to $D_1 + e^-$ during the $S_2 \rightarrow S_1$ internal conversion. The dashed arrows indicate the most probable ionization channels. Figure reproduced from ref. 101 with minor corrections.

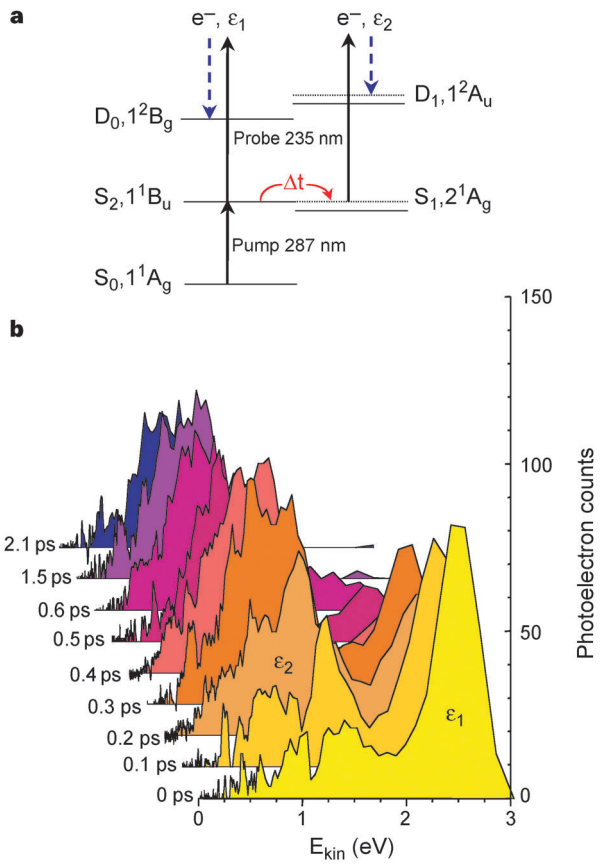

Fig. 11 Time-resolved vibrational and electronic dynamics during internal conversion in DT. (a) Level scheme in DT for one-photon probe ionization. The pump laser prepares the optically bright state S_2. Due to ultrafast internal conversion, this state converts to the lower-lying state S_1 with 0.7 eV of vibrational energy. The expected ionization propensity rules, according to Fig. 10, are shown: $S_2 \rightarrow D_0 + e^-$ (ε_1) and $S_1 \rightarrow D_1 + e^-$ (ε_2). (b) Femtosecond time-resolved photoelectron kinetic energy (E_{kin}) spectra of DT pumped at 287 nm and probed at 235 nm. There is a rapid shift (~400 fs) in the distribution: from (ε_1), an energetic peak at 2.5 eV due to photoionization of S_2 into the D_0 cation ground electronic state; to (ε_2), a broad, structured band at lower energies due to photoionization of vibrationally hot S_1 into the D_1 cation first excited electronic state. The structure in the lower energy band reflects the vibrational dynamics in S_1. The time delay between the pump (excitation) and the probe (ionization) laser pulses is indicated by Δt. Figure reproduced from ref. 101.

(ε_1 = 2.5 eV) to a broad, structured low-energy band (ε_2). This is the direct signature of the evolving electronic character induced by non-adiabatic coupling. The ε_1 band is due to ionization of the S_2 state into the D_0 ion state. The ε_2 band arises from photoionization of the S_1 state that correlates with the D_1 ion state: its appearance is due to population of the S_1 state by internal conversion. Integration of the photoelectron bands gives an S_2 to S_1 internal conversion timescale of 386 ± 65 fs.

The above is an example of disentangling the electronic from vibrational dynamics using TRPES in the favorable complementary photoionization case. In the corresponding ionization correlations case, the geometry changes upon non-adiabatic crossing and ionization will strongly affect the ability to disentangle electronic from vibrational dynamics. In some cases,[49] we are still able to directly monitor the non-adiabatic processes. However, in general, this correspondence hinders the disentangling of the electronic population dynamics from the nuclear dynamics. In such cases, PADs[26,102,103] should in general still change during a non-adiabatic process, providing information on the electronic symmetry of the evolving state. In the following section, we will discuss the application of TRPADs to studies of non-adiabatic processes in excited polyatomic molecules.

3.2.3 Time-resolved coincidence imaging spectroscopy: femtochemistry from the molecule's point of view. Time- and energy-resolved photoelectron spectra alone may not always provide detailed enough information on intrinsically coupled electronic and nuclear motions due to the strong overlap of FC spectra. The TRPAD, on the other hand, in general provides additional information about the evolving electronic character, which is often complementary to the information obtained from the time- and energy-resolved measurements. However, measurements are usually made in the laboratory frame, where averaging over the random orientation of the molecule generally leads to a loss of information. Ideally, one would prefer to observe these dynamics from the molecule's point of view (the molecular frame) rather than the laboratory point of view. One method to realize this is to prealign polyatomic molecules before studying their field-free dynamics.[69,104–106] Another approach to molecular frame observables is time-resolved coincidence imaging spectroscopy (TRCIS), which measures fully correlated photofragment and photoelectron recoil distributions as a function of time. In the favorable case of axial recoil, the fragments are emitted along the breaking bond. The recoil direction of fragment therefore provides information on the orientation of the molecule (except the azimuthal angle about the recoil axis) at the moment of ionization. This permits dynamical observations from the molecule's point of view. Here, we discuss the ultraviolet (UV) photodissociation of the nitric oxide dimer as an example of femtochemistry from the molecule's point of view. Further details can be found in ref. 107 and references therein.

The nitric oxide dimer $(NO)_2$ has a *cis*-planar (C_{2v}) structure (Fig. 12). The broad and diffuse UV absorption spectrum arises from a parallel transition (parallel to the N–N bond) to an ill-characterized dissociative continuum (depicted as a gray box). The dissociation yields both the ground state and first

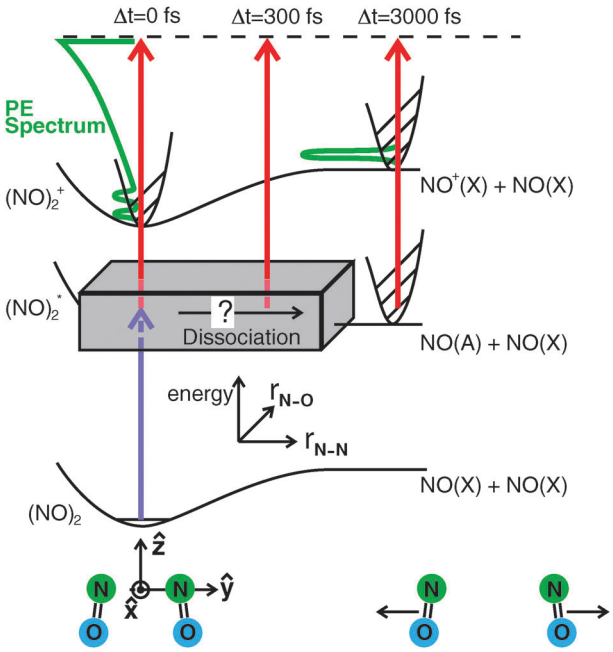

Fig. 12 Schematic representation of the femtosecond pump–probe TRPES study of the NO dimer dissociation dynamics. The gray box represents the complex region the molecule must pass through upon UV photodissociation into NO(A) + NO(X). The TRPES method monitors the complete time evolution of the excited state. The molecular frame axis convention is shown (bottom), with the *y* axis along the N–N bond. The purple arrow represents the pump (excitation) laser photon. The red arrows represent the probe (ionization) laser photon that interrogates the evolving excited state, shown here at three selected time delays. The green curves represent the photoelectron kinetic energy (PE) spectrum observed after ionization at these time delays. Figure reproduced from ref. 107.

excited state NO monomer fragments. The latter has dominant Rydberg 3s orbital character. Neither the featureless absorption spectrum nor the apparently statistical product-state distributions offer much insight into the dynamics. More detailed product-state distributions of $(NO)_2$ at excitation energy just above the NO(A 3s) channel threshold confirm that the photofragment recoil direction is strongly peaked parallel to the pump laser polarization and that the excited molecule retains planar geometry during dissociation.

Ab initio studies offered some information about the electronically excited states of $(NO)_2$. One study established that there exist states in the gray region of Fig. 12 that are of B_2 symmetry; these states consist of a diffuse $3p_y$ Rydberg state (*y* axis along the N–N bond) and a localized valence state of charge transfer character that carries the oscillator strength.

In the experiment, a supersonic molecular beam source (15% NO in He) produced cold $(NO)_2$, which was pumped by femtosecond pulses at 209.6 nm (above the NO(A 3s) channel threshold) and probed, *via* single-photon ionization, with femtosecond pulses at 279.5 nm. The pump and probe laser polarizations were parallel to each other. The dynamics were measured in two independent pump–probe experiments. High-resolution time- and energy-resolved spectra were recorded with TRPES, whereas three-dimensional (3D) energy- and

angle-resolved photoelectron–photoion correlations were measured by TRCIS at five specific time delays.

TRPES follows the whole dynamic process, from the initial excitation ($\Delta t = 0$), through the intermediate state (gray box in Fig. 12), to the final products ($\Delta t > 3000$ fs). The TRPES data are shown in Fig. 13. A nonlinear fitting procedure was used to globally fit the data at all photoelectron energies and time delays simultaneously. These data cannot be fit by single-exponential kinetics. They are fit with high accuracy by a two-step sequential model, meaning that an initial bright state $(NO)_2^*$ evolves to an intermediate configuration, which itself subsequently decays to yield free NO(A 3s) + NO(X) products. The decay time of the initial state is 140 ± 30 fs, which matches the rise time of the intermediate configuration. This intermediate configuration has a subsequent decay time of 590 ± 20 fs.

To identify this intermediate configuration, the TRCIS method was applied. The pump transition dipole is along the molecular frame y axis, the N–N bond axis (see Fig. 12). The pump transition therefore forms an anisotropic distribution of excited $(NO)_2^*$ states in the lab frame, with the N–N bond aligned along the laser polarization axis. The dissociative ionization of $(NO)_2^*$ produces NO^+ fragments strongly directed along the laser polarization axis. The NO^+ fragment recoil direction therefore indicates the lab frame direction of the N–N bond (molecular frame y axis) before ionization. Rotating the electron momentum vector into the fragment recoil frame on an event-by-event basis allows for reconstruction of the $(NO)_2^*$ photoelectron angular distribution in this recoil frame, rather than the usual lab frame. Here the recoil frame coincides with the molecular frame, differing only by azimuthal averaging about the N–N bond. Out of all fragment recoil events, only those directed ("up" or "down") along the parallel pump and probe laser polarization axis were selected. By choosing events from this selected set, the data were restricted to excited-state ionization events arising from interactions with the y component of the ionization transition dipole alone ($\Gamma_{\text{dipole}} = \Gamma_y = B_2$). This restriction greatly limits the allowed partial waves for the emitted electron, especially in the present case where only a single electronic continuum is accessed (due to the symmetry reason, as discussed in Section 2.5.2). In Fig. 14, time-resolved lab and recoil frame photoelectron angular distributions arising from photoionization of $(NO)_2^*$ in the 9.9 to 10.3 eV band of Fig. 13 are presented. This band contains significant contributions from the intermediate configuration, as shown by the data fitting. The lab frame photoelectron angular distributions have a largely isotropic character that shows little time evolution due to the averaging over the random orientation of ground state $(NO)_2$, obscuring the excited state dynamics. By contrast, the recoil frame PADs show a highly anisotropic character and a variation with time delay. The solid lines in the polar plots of Fig. 14 are fits to Legendre polynomials (see eqn (21)), with even-order Legendre polynomials $P_L(\theta)$ up to $L = 4$ for the lab frame and up to $L = 8$ for the recoil frame. The recoil frame PADs have dominant intensity perpendicular to the laser polarization axis. The ground state of cation has A_1 symmetry. From symmetry arguments (see eqn (25)), an A_1 Rydberg intermediate state leads to photoelectrons of B_2 symmetry, which would most likely have maximum intensity

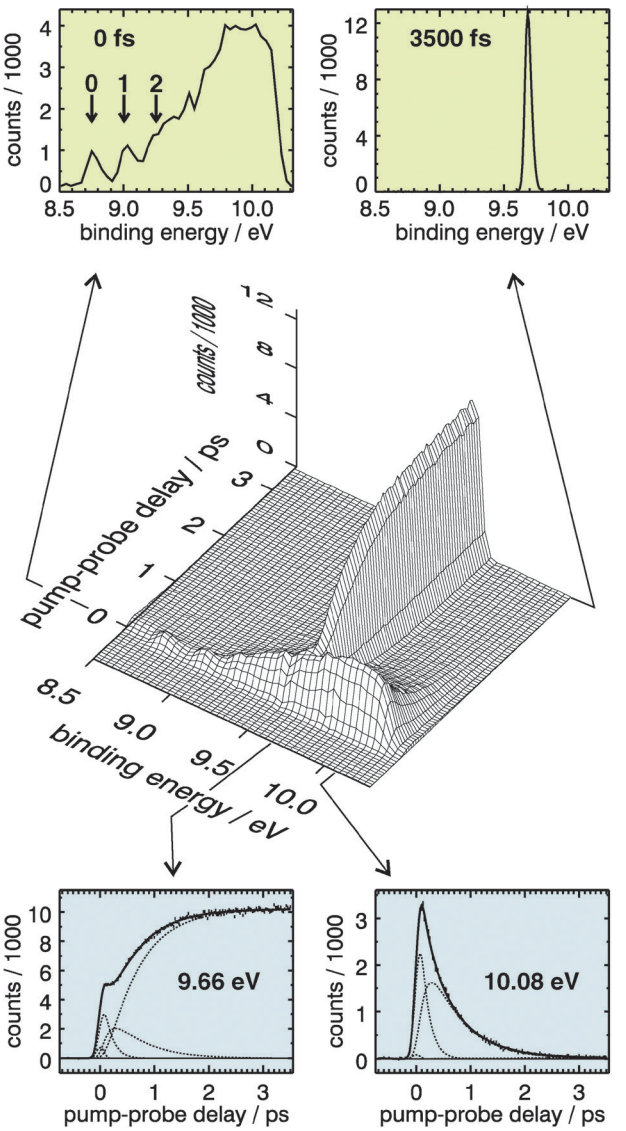

Fig. 13 A TRPES scan showing photoelectron spectra as a function of time delay in a 2D plot. The binding energy is the total photon energy (pump plus probe) minus the electron kinetic energy. The green insets (top) are examples of photoelectron spectra at two time delays. The blue insets (bottom) are examples of the evolution of the photoelectron intensity at two binding energies. Note that the 2D data are globally fit at all energies and time delays simultaneously. The solid lines in the blue graphs are from the 2D fits to a sequential two-step dissociation model. The dotted lines are the respective initial, intermediate, and final state signal components plus a small instrumental response contribution. Figure reproduced from ref. 107.

parallel to the laser polarization axis, in contrast to what is observed. This rules out the A_1 Rydberg 3s state as the intermediate configuration.

A semiquantitative analysis of these MF TRPADs was also performed in ref. 107. Ionization of a B_2 electronic state to an A_1 cation state *via* a y-polarized transition means that the free electron must have A_1 symmetry. The A_1 symmetry partial waves are sσ, pσ, dσ, dδ, fσ, fδ, gσ, gδ, and gγ.... In the modeling of the data, only s, p, d, f and g partial waves were used because the maximum order of Legendre polynomials

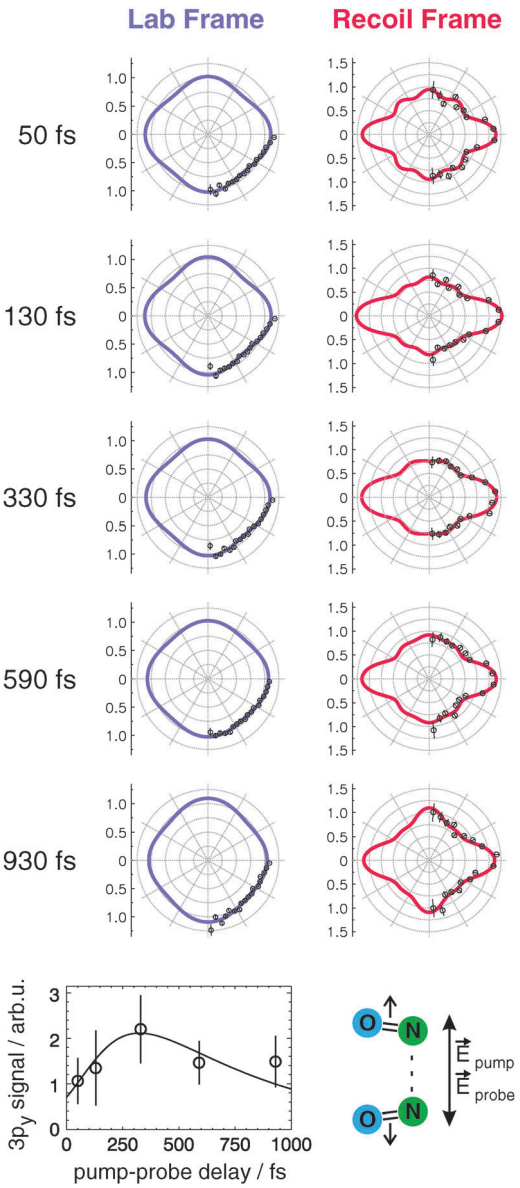

Fig. 14 TRCIS data showing lab frame (left) and recoil frame (right) photoelectron angular distributions (PADs) from the 9.9 to 10.3 eV dissociative ionization region of Fig. 13. The laser polarizations and recoil frame axes are along the y direction, as shown (bottom right). The lab frame PADs show featureless and almost invariant behavior. The recoil frame PADs show strong anisotropies that vary with time. The fit curves (solid lines) include even-order Legendre polynomials $P_L(\theta)$ up to $L = 4$ for the lab frame and up to $L = 8$ for the recoil frame. The average partial wave contribution expected from Rydberg $3p_y$ ionization is plotted at the lower left as a function of time. The time dependence of the intermediate configuration extracted from Fig. 13 is plotted here as the solid line, agreeing very well with the time dependence of the $3p_y$ ionization contribution. This confirms the intermediate configuration as being of Rydberg $3p_y$ character. Figure reproduced from ref. 107.

needed in the recoil frame TRPADs fitting is $L_{max} = 8$ (maximum angular momentum $l_{max} = \frac{L_{max}}{2} = 4$). All partial waves were contracted into two sets: those expected from $3p_y$ ionization and those not. Ionization of a dimer $3p_y$ Rydberg state *via* a y-polarized transition would produce only electrons with sσ, dσ, and dδ character. Therefore, the ratio of (sσ + dσ + dδ) to the sum of all other contributions (Σpfg) is a measure of $3p_y$ Rydberg character in the $(NO)_2^*$ excited electronic states. At the bottom of Fig. 14, the time dependence of this ratio is plotted, labeled "$3p_y$ signal"; this plot shows that dimer $3p_y$ Rydberg character rises from early times, peaks at ~330 fs, and subsequently falls. The solid curve is the time dependence of the intermediate configuration extracted from Fig. 13, showing that the $3p_y$ character follows the time behavior of the intermediate configuration. The agreement substantiates the intermediate configuration as being of $3p_y$ character.

The dynamics of excited polyatomic molecules generally involves the complex mixing of electronic states. The above example shows how TRCIS reveals new details on the evolution of the excited states from molecular frame measurements which cannot be extracted from lab frame measurements alone.

4 Conclusions and outlook

TRPES is a powerful probe in studies of non-adiabatic dynamics in isolated polyatomic molecules because photoelectron spectroscopy is sensitive to both electronic configurations and vibrational dynamics, due to Koopmans' correlations and FC overlaps, respectively. Therefore, the time- and energy-resolved photoelectron spectrum permits monitoring of both electronic population dynamics and vibrational dynamics, disentangling them in favorable cases. The molecular frame TRPAD is sensitive to the electronic character (symmetry) of the evolving wavepacket, providing information complementary to time- and energy-resolved photoelectron spectroscopy measurements.

Although the theory discussed here has been well known for many years, recent developments in both experimental techniques and computational methods have made application of these concepts to ultrafast non-adiabatic dynamics of polyatomic molecules increasingly realistic. For example, modern alignment techniques combined with 3D photoelectron imaging have enabled the observation of TRPADs in the molecular frame.[69,71] These results, combined with symmetry-based modeling, provided a paradigmatic example of the application of the B–O framework to photoionization. In this case, the nuclear and electronic dynamics are mapped onto the TRPES and TRPADs, respectively, providing observables which disentangle the coupled non-adiabatic dynamics. Such insights are key to gaining a deeper understanding of non-adiabatic processes in small polyatomics and, just as importantly, understanding how such dynamics are mapped in TRPES experiments. Application of these techniques to larger molecules is fast becoming a reasonable proposition.

Ab initio methods which combine both excited state dynamics and accurate photoionization calculations are now becoming feasible for polyatomics. Such methods are very powerful, providing the means to separate and investigate every aspect of the excited state dynamics and their respective contributions to the observed TRPES and TRPADs, but require a significant computational effort. The state-of-the-art is represented by calculations on the dynamics of NO_2 at a conical intersection,[46] which includes full treatment of the pump and probe laser pulses,

the multi-dimensional dynamics on the non-adiabatically coupled excited state surfaces, and the energy and geometry dependent photoionization matrix elements. A computationally cheaper approach is offered by dynamics calculations which are "on-the-fly", such as *ab initio* multiple spawning (AIMS).[108] In this approach full multi-dimensional surfaces are not calculated prior to wavepacket dynamics, instead points on the surfaces are calculated only when required by the propagation of the wavepacket, thus significantly decreasing the computational cost for calculations on polyatomic molecules. Such "on-the-fly" methods, once combined with accurate calculation of observables, therefore present an approach which should scale up to larger polyatomics. The first steps in this direction, with the energy- and time-resolved photoelectron spectrum as the observable, have begun.[109]

We hope that, through investigation of prototypical cases, we will develop understanding of, and intuition about, excited state dynamics, perhaps leading to different types or classes of wavepacket behaviour and enabling complex experimental data to be interpreted qualitatively or semi-quantitatively with the aid of model calculations. Although the investigation of non-adiabatic excited state dynamics presents a significant experimental and theoretical challenge, the key role of such dynamics in photoinduced processes, not least in large biological molecules, demands that this challenge is met. The increasing availability of femtosecond laser systems and photoelectron imaging apparatus make this an exciting time from the experimental perspective, while the development of *ab initio* dynamics methods and their consolidation with accurate photoionization calculations[110] brings an increasing maturity to TRPES theory and computation. As experiment and theory continue to develop and grow together, the outlook for time-resolved photoelectron spectroscopy of excited state chemical reactions appears most promising.

Acknowledgements

We thank Owen Clarkin, Jonny Midgley and Katharine Reid for helpful discussions.

References

1 M. Bixon and J. Jortner, *J. Chem. Phys.*, 1968, **48**, 715–726.
2 J. Jortner, S. A. Rice and R. M. Hochstrasser, in *Adv. Photochem.*, ed. J. N. Pitts, G. S. Hammond and W. A. Noyes, John Wiley & Sons, Inc., 2007, vol. 7, ch. Radiationless Transitions in Photochemistry, pp. 149–309.
3 B. R. Henry and W. Siebrand, in *Organic Molecular Photophysics*, ed. J. B. Birks, John Wiley & Sons, 1973, vol. 1, ch. Radiationless transitions, pp. 153–237.
4 G. A. Worth and L. S. Cederbaum, *Annu. Rev. Phys. Chem.*, 2004, **55**, 127–158.
5 H. Köppel, W. Domcke and L. S. Cederbaum, in *Adv. Chem. Phys.*, John Wiley & Sons, Inc., 2007, ch. Multimode Molecular Dynamics Beyond the Born–Oppenheimer Approximation, pp. 59–246.
6 W. Domcke and G. Stock, in *Advances in Chemical Physics*, ed. I. Prigogine and S. A. Rice, John Wiley & Sons, Inc., 1997, vol. 100, ch. Theory of Ultrafast Nonadiabatic Excited-State Processes and their Spectroscopic Detection in Real Time, pp. 1–169.
7 J. Michl and V. Bonacic-Koutecky, *Electronic Aspects of Organic Photochemistry*, Wiley-Interscience, 1990.
8 R. Schoenlein, L. Peteanu, R. Mathies and C. Shank, *Science*, 1991, **254**, 412–415.
9 L. Hammarström and S. Styring, *Philos. Trans. R. Soc. London, Ser. B*, 2008, **363**, 1283–1291.
10 M. Dantus, M. J. Rosker and A. H. Zewail, *J. Chem. Phys.*, 1987, **87**, 2395–2397.
11 T. S. Rose, M. J. Rosker and A. H. Zewail, *J. Chem. Phys.*, 1988, **88**, 6672–6673.
12 A. H. Zewail, *J. Phys. Chem. A*, 2000, **104**, 5660–5694.
13 J. C. Williamson, J. Cao, H. Ihee, H. Frey and A. H. Zewail, *Nature*, 1997, **386**, 159–162.
14 C. Rischel, A. Rousse, I. Uschmann, P.-A. Albouy, J.-P. Geindre, P. Audebert, J.-C. Gauthier, E. Froster, J.-L. Martin and A. Antonetti, *Nature*, 1997, **390**, 490–492.
15 A. H. Chin, R. W. Schoenlein, T. E. Glover, P. Balling, W. P. Leemans and C. V. Shank, *Phys. Rev. Lett.*, 1999, **83**, 336–339.
16 C. W. Siders, A. Cavalleri, K. Sokolowski-Tinten, C. Tóth, T. Guo, M. Kammler, M. H. v. Hoegen, K. R. Wilson, D. v. d. Linde and C. P. J. Barty, *Science*, 1999, **286**, 1340–1342.
17 J. R. Dwyer, C. T. Hebeisen, R. Ernstorfer, M. Harb, V. B. Deyirmenjian, R. E. Jordan and R. Dwayne Miller, *Philos. Trans. R. Soc. London, Ser. A*, 2006, **364**, 741–778.
18 M. Eichberger, H. Schafer, M. Krumova, M. Beyer, J. Demsar, H. Berger, G. Moriena, G. Sciaini and R. J. D. Miller, *Nature*, 2010, **468**, 799–802.
19 J. H. D. Eland, *Photoelectron Spectroscopy*, Butterworths, 2nd edn, 1985.
20 I. Fischer, D. M. Villeneuve, M. J. J. Vrakking and A. Stolow, *J. Chem. Phys.*, 1995, **102**, 5566–5569.
21 C. C. Hayden and A. Stolow, in *Photoionization and Photodetachment*, ed. C.-Y. Ng, World Scientific Publishing Company, 2000, vol. 10A, ch. Non-Adiabatic Dynamics Studied by Femtosecond Time-Resolved Photoelectron Spectroscopy, pp. 91–126.
22 W. Radloff, in *Photoionization and Photodetachment*, ed. C.-Y. Ng, World Scientific Publishing Company, 2000, vol. 10A, ch. Femtosecond Time-Resolved Photoelectron Spectroscopy of Molecules and Clusters by Photoion-Photoelectron Coincidence Detection, pp. 127–181.
23 K. Takatsuka, Y. Arasaki, K. Wang and V. McKoy, *Faraday Discuss.*, 2000, **115**, 1–15.
24 D. M. Neumark, *Annu. Rev. Phys. Chem.*, 2001, **52**, 255–277.
25 T. Suzuki and B. J. Whitaker, *Int. Rev. Phys. Chem.*, 2001, **20**, 313–356.
26 T. Seideman, *Annu. Rev. Phys. Chem.*, 2002, **53**, 41–65.
27 K. L. Reid, *Annu. Rev. Phys. Chem.*, 2003, **54**, 397–424.
28 A. Stolow, *Annu. Rev. Phys. Chem.*, 2003, **54**, 89–119.
29 A. Stolow, A. E. Bragg and D. M. Neumark, *Chem. Rev.*, 2004, **104**, 1719–1758.
30 M. Wollenhaupt, V. Engel and T. Baumert, *Annu. Rev. Phys. Chem.*, 2005, **56**, 25–56.
31 T. Suzuki, *Annu. Rev. Phys. Chem.*, 2006, **57**, 555–592.
32 I. V. Hertel and W. Radloff, *Rep. Prog. Phys.*, 2006, **69**, 1897.
33 A. Stolow and J. G. Underwood, in *Adv. Chem. Phys.*, ed. S. A. Rice, John Wiley & Sons, Inc., 2008, vol. 39, ch. Time-Resolved Photoelectron Spectroscopy of Nonadiabatic Dynamics in Polyatomic Molecules, pp. 497–584.
34 *Conical Intersections: Electronic Structure, Dynamics & Spectroscopy*, ed. W. Domcke, D. R. Yarkony and H. Köppel, World Scientific, 2004.
35 Y. Arasaki, K. Takatsuka, K. Wang and V. McKoy, *Chem. Phys. Lett.*, 1999, **302**, 363–374.
36 Y. Arasaki, K. Takatsuka, K. Wang and V. McKoy, *J. Chem. Phys.*, 2000, **112**, 8871–8884.
37 M. Seel and W. Domcke, *Chem. Phys.*, 1991, **151**, 59–72.
38 V. Blanchet, S. Lochbrunner, M. Schmitt, J. P. Shaffer, J. J. Larsen, M. Z. Zgierski, T. Seideman and A. Stolow, *Faraday Discuss.*, 2000, **115**, 33–48.
39 K. F. Freed, in *Radiationless Processes in Molecule and Condensed Phase*, ed. F. K. Fong, Springer-Verlag, 1976, ch. Energy Dependence of Electronic Relaxation Processes in Polyatomic Molecules, pp. 23–168.
40 P. R. Bunker and P. Jensen, *Molecular Symmetry and Spectroscopy*, NRC Research Press, Ottawa, 2nd edn, 1998.
41 J. G. Underwood and K. L. Reid, *J. Chem. Phys.*, 2000, **113**, 1067–1074.
42 K. L. Reid and J. G. Underwood, *J. Chem. Phys.*, 2000, **112**, 3643–3649.

43 E. J. Heller, *Acc. Chem. Res.*, 1981, **14**, 368–375.
44 F. K. Fong, in *Radiationless Processes in Molecule and Condensed Phase*, ed. F. K. Fong, Springer-Verlag, 1976, ch. Introduction, pp. 1–21.
45 J. C. Tully, *J. Chem. Phys.*, 1990, **93**, 1061–1071.
46 Y. Arasaki, K. Takatsuka, K. Wang and V. McKoy, *J. Chem. Phys.*, 2010, **132**, 124307.
47 T. Azumi and K. Matsuzaki, *Photochem. Photobiol.*, 1977, **25**, 315–326.
48 V. Blanchet, M. Z. Zgierski and A. Stolow, *J. Chem. Phys.*, 2001, **114**, 1194–1205.
49 M. Schmitt, S. Lochbrunner, J. P. Shaffer, J. J. Larsen, M. Z. Zgierski and A. Stolow, *J. Chem. Phys.*, 2001, **114**, 1206–1213.
50 K. L. Reid, *Int. Rev. Phys. Chem.*, 2008, **27**, 607–628.
51 E. J. Heller, *J. Chem. Phys.*, 1975, **62**, 1544–1555.
52 A. Stolow, *Philos. Trans. R. Soc. London, Ser. A*, 1998, **356**, 345–362.
53 *The Physics and Chemistry of Wave Packets*, ed. J. A. Yeazell and T. Uzer, Wiley-Interscience, 2000.
54 V. Engel and H. Metiu, *J. Chem. Phys.*, 1989, **90**, 6116–6128.
55 E. J. Heller, *J. Chem. Phys.*, 1976, **64**, 63–73.
56 Y. Arasaki, K. Takatsuka, K. Wang and V. McKoy, *J. Electron Spectrosc. Relat. Phenom.*, 2000, **108**, 89–98.
57 A. Assion, M. Geisler, J. Helbing, V. Seyfried and T. Baumert, *Phys. Rev. A: At., Mol., Opt. Phys.*, 1996, **54**, R4605–R4608.
58 R. de Nalda, J. Dura, A. Garcia-Vela, J. G. Izquierdo, J. Gonzalez-Vazquez and L. Banares, *J. Chem. Phys.*, 2008, **128**, 244309.
59 L. Rubio-Lago, A. Garcia-Vela, A. Arregui, G. A. Amaral and L. Banares, *J. Chem. Phys.*, 2009, **131**, 174309.
60 J. A. Davies, A. M. Green and K. L. Reid, *Phys. Chem. Chem. Phys.*, 2010, **12**, 9872–9883.
61 S. N. Dixit and V. McKoy, *J. Chem. Phys.*, 1985, **82**, 3546–3553.
62 T. Seideman, *Phys. Rev. A: At., Mol., Opt. Phys.*, 2001, **64**, 042504.
63 J. Tellinghuisen, in *Advances in Chemical Physics*, ed. K. P. Lawley, John Wiley & Sons, Inc., 1985, vol. 60, ch. The Franck–Condon Principle in Bound-Free Transitions, pp. 299–369.
64 I. Fischer, M. Vrakking, D. Villeneuve and A. Stolow, *Chem. Phys.*, 1996, **207**, 331–354.
65 K. Resch, V. Blanchet, A. Stolow and T. Seideman, *J. Phys. Chem. A*, 2001, **105**, 2756–2763.
66 C. N. Yang, *Phys. Rev.*, 1948, **74**, 764–772.
67 K. L. Reid, D. J. Leahy and R. N. Zare, *J. Chem. Phys.*, 1991, **95**, 1746–1756.
68 D. Dill, *J. Chem. Phys.*, 1976, **65**, 1130–1133.
69 C. Z. Bisgaard, O. J. Clarkin, G. Wu, A. M. D. Lee, O. Gessner, C. C. Hayden and A. Stolow, *Science*, 2009, **323**, 1464–1468.
70 R. Signorell and F. Merkt, *Mol. Phys.*, 1997, **92**, 793–804.
71 P. Hockett, C. Z. Bisgaard, O. J. Clarkin and A. Stolow, *Nat. Phys.*, 2011, **7**, 612–615.
72 J. Lecointre, G. M. Roberts, D. A. Horke and J. R. R. Verlet, *J. Phys. Chem. A*, 2010, **114**, 11216–11224.
73 A. Messiah, *Quantum Mechanics Volume I*, North-Holland Publishing Company, 1970.
74 U. Fano and A. R. P. Rau, *Atomic Collisions and Spectra*, Academic Press Inc., 1986.
75 J. Cooper and R. N. Zare, in *Lectures in Theoretical Physics: Atomic Collision Processes*, ed. K. T. M. S. Geltman and W. E. Brittin, Gordon and Breach, New York, 1969, vol. XI–C, ch. Photoelectron Angular Distributions, pp. 317–337.
76 H. Park and R. N. Zare, *J. Chem. Phys.*, 1996, **104**, 4554–4567.
77 J. Cooper and R. N. Zare, *J. Chem. Phys.*, 1968, **48**, 942–943.
78 R. N. Zare, *Angular Momentum: Understanding spatial aspects in chemistry and physics*, John Wiley & Sons, 1988.
79 W. J. Thompson, *Angular Momentum*, Wiley-Interscience, 1994.
80 R. R. Lucchese, *J. Electron Spectrosc. Relat. Phenom.*, 2004, **141**, 201–210.
81 K. Mller-Dethlefs, M. Sander and E. W. Schlag, *Chem. Phys. Lett.*, 1984, **112**, 291–294.
82 K. Muller-Dethlefs and E. W. Schlag, *Annu. Rev. Phys. Chem.*, 1991, **42**, 109–136.
83 M. C. R. Cockett, *Chem. Soc. Rev.*, 2005, **34**, 935–948.
84 C. A. de Lange, in *High resolution Laser Photoionization and Photoelectron Studies*, ed. C. Y. N. I. Powis and T. Baer, Wiley, 1995, p. 195.
85 S. Lochbrunner, J. J. Larsen, J. P. Shaffer, M. Schmitt, T. Schultz, J. G. Underwood and A. Stolow, *J. Electron Spectrosc. Relat. Phenom.*, 2000, **112**, 183–198.
86 A. T. J. B. Eppink and D. H. Parker, *Rev. Sci. Instrum.*, 1997, **68**, 3477–3484.
87 L. Wang, H. Kohguchi and T. Suzuki, *Faraday Discuss.*, 1999, **113**, 37–46.
88 J. A. Davies, J. E. LeClaire, R. E. Continetti and C. C. Hayden, *J. Chem. Phys.*, 1999, **111**, 1–4.
89 R. E. Continetti, *Annu. Rev. Phys. Chem.*, 2001, **52**, 165–192.
90 W. Radloff, V. Stert, T. Freudenberg, I. Hertel, C. Jouvet, C. Dedonder-Lardeux and D. Solgadi, *Chem. Phys. Lett.*, 1997, **281**, 20–26.
91 J. M. Smith, C. Lakshminarayan and J. L. Knee, *J. Chem. Phys.*, 1990, **93**, 4475–4476.
92 T. Baumert, R. Thalweiser and G. Gerber, *Chem. Phys. Lett.*, 1993, **209**, 29–34.
93 J. Vallerga, G. Kaplan, O. Siegmund, M. Lampton and R. Malina, *IEEE Trans. Nucl. Sci.*, 1989, **36**, 881–886.
94 J. V. Vallerga and O. H. W. Siegmund, *Nucl. Instrum. Methods Phys. Res., Sect. A*, 2000, **442**, 159–163.
95 O. Siegmund, A. Tremsin, J. Vallerga and J. Hull, *IEEE Trans. Nucl. Sci.*, 2001, **48**, 430–434.
96 J. A. Davies, R. E. Continetti, D. W. Chandler and C. C. Hayden, *Phys. Rev. Lett.*, 2000, **84**, 5983–5986.
97 V. Blanchet and A. Stolow, *J. Chem. Phys.*, 1998, **108**, 4371–4374.
98 D. R. Cyr and C. C. Hayden, *J. Chem. Phys.*, 1996, **104**, 771–774.
99 B. Kim, C. P. Schick and P. M. Weber, *J. Chem. Phys.*, 1995, **103**, 6903–6913.
100 J. Jortner, S. A. Rice and R. M. Hochstrasser, in *Advances in Photochemistry*, ed. J. N. Pitts, G. S. Hammond and K. Gollnick, Wiley, 1969, vol. 7, pp. 149.
101 V. Blanchet, M. Z. Zgierski, T. Seideman and A. Stolow, *Nature*, 1999, **401**, 52–54.
102 K. L. Reid, S. P. Duxon and M. Towrie, *Chem. Phys. Lett.*, 1994, **228**, 351–356.
103 T. Seideman, *J. Chem. Phys.*, 1997, **107**, 7859–7868.
104 H. Stapelfeldt and T. Seideman, *Rev. Mod. Phys.*, 2003, **75**, 543–557.
105 J. G. Underwood, B. J. Sussman and A. Stolow, *Phys. Rev. Lett.*, 2005, **94**, 143002.
106 T. P. Rakitzis, A. J. van den Brom and M. H. M. Janssen, *Science*, 2004, **303**, 1852–1854.
107 O. Gessner, A. M. D. Lee, J. P. Shaffer, H. Reisler, S. V. Levchenko, A. I. Krylov, J. G. Underwood, H. Shi, A. L. L. East, D. M. Wardlaw, E. t. H. Chrysostom, C. C. Hayden and A. Stolow, *Science*, 2006, **311**, 219–222.
108 M. Ben-Nun and T. J. Martínez, in *Advances in Chemical Physics*, John Wiley & Sons, Inc., 2002, vol. 121, ch. *Ab initio* Quantum Molecular Dynamics, pp. 439–512.
109 H. R. Hudock, B. G. Levine, A. L. Thompson, H. Satzger, D. Townsend, N. Gador, S. Ullrich, A. Stolow and T. J. Martínez, *J. Phys. Chem. A*, 2007, **111**, 8500–8508.
110 M. S. Schuurman, and T. J. Martinez, private communication.